

Review

# Recent Progress in Cathode-Free Zinc Electrolytic MnO<sub>2</sub> Batteries: Electrolytes and Electrodes

Shiwei Liu <sup>1,2</sup>, Zhongqi Liang <sup>1</sup>, Hang Zhou <sup>1</sup> , Weizheng Cai <sup>3</sup>, Jiazen Wu <sup>3</sup> , Qianhui Zhang <sup>4</sup>, Guoshen Yang <sup>5</sup>, Walid A. Daoud <sup>6</sup> , Zanxiang Nie <sup>2</sup>, Pritesh Hirralal <sup>2</sup>, Shiqiang Luo <sup>2,\*</sup>  and Gehan A. J. Amaratunga <sup>2,7,8,\*</sup> 

<sup>1</sup> School of Electronic and Computer Engineering, Peking University Shenzhen Graduate School, Shenzhen 518055, China

<sup>2</sup> Zinergy Shenzhen Ltd., Gangzhilong Science Park, Shenzhen 518110, China

<sup>3</sup> Department of Materials Science and Engineering, Southern University of Science and Technology, Shenzhen 518055, China

<sup>4</sup> School of Microelectronics Science and Technology, Sun Yat-Sen University, Guangzhou 510275, China

<sup>5</sup> School of Information Science and Engineering, Shandong University, 72 Binhai Road, Qingdao 266237, China

<sup>6</sup> Department of Mechanical Engineering, City University of Hong Kong, Kowloon, Hong Kong 999077, China

<sup>7</sup> Department of Engineering, Electrical Engineering Division, University of Cambridge, 9 JJ Thomson Avenue, Cambridge CB3 0FA, UK

<sup>8</sup> Institute of Critical Materials for Integrated Circuits, Shenzhen Polytechnic University, Shenzhen 518055, China

\* Correspondence: luoshiqiang@zinergy-power.cn (S.L.); gaja1@cam.ac.uk (G.A.J.A.)

**Abstract:** Zinc–manganese dioxide (Zn–MnO<sub>2</sub>) batteries, pivotal in primary energy storage, face challenges in rechargeability due to cathode dissolution and anode corrosion. This review summarizes cathode-free designs using pH-optimized electrolytes and modified electrodes/current collectors. For electrolytes, while acidic systems with additives (PVP, HAc) enhance ion transport, dual-electrolyte configurations (ion-selective membranes/hydrogels) reduce Zn corrosion. Near-neutral strategies utilize nanomicelles/complexing agents to regulate MnO<sub>2</sub> deposition. Moreover, mediators (I<sup>−</sup>, Br<sup>−</sup>, Cr<sup>3+</sup>) reactivate MnO<sub>2</sub> but require shuttle-effect control. For the electrodes/current collectors, electrode innovations including SEI/CEI layers and surfactant-driven phase tuning are introduced. Electrode-free designs and integrated “supercapattery” systems combining supercapacitors with Zn–MnO<sub>2</sub>/I<sub>2</sub> chemistries are also discussed. This review highlights electrolyte–electrode synergy and hybrid device potential, paving the way for sustainable, high-performance Zn–MnO<sub>2</sub> systems.



Academic Editor: Johan E. ten Elshof

Received: 13 March 2025

Revised: 15 April 2025

Accepted: 22 April 2025

Published: 23 April 2025

**Citation:** Liu, S.; Liang, Z.; Zhou, H.; Cai, W.; Wu, J.; Zhang, Q.; Yang, G.; Daoud, W.A.; Nie, Z.; Hirralal, P.; et al.

Recent Progress in Cathode-Free Zinc Electrolytic MnO<sub>2</sub> Batteries: Electrolytes and Electrodes. *Batteries* **2025**, *11*, 171. <https://doi.org/10.3390/batteries11050171>

**Copyright:** © 2025 by the authors. Licensee MDPI, Basel, Switzerland. This article is an open access article distributed under the terms and conditions of the Creative Commons Attribution (CC BY) license (<https://creativecommons.org/licenses/by/4.0/>).

## 1. Introduction

Zinc–manganese dioxide (MnO<sub>2</sub>) batteries continue to dominate the primary battery market, making efforts to render them rechargeable highly promising [1]. However, rechargeable alkaline Zn–MnO<sub>2</sub> batteries have historically suffered from poor cycling performance, prompting recent research to focus on near-mild acidic or neutral electrolytes [1,2]. Although the first report of a Zn// $\gamma$ -MnO<sub>2</sub> battery using a mild acidic ZnSO<sub>4</sub> electrolyte dates back to 1988 [3], widespread attention emerged only in 2012 when Zn// $\alpha$ -MnO<sub>2</sub> demonstrated excellent reversibility and cyclability, as illustrated in Figure 1a [4]. Initially, the electrochemical mechanism was attributed to Zn<sup>2+</sup> ion (de)intercalation, facilitated by the large 2 × 2 tunnel structure of  $\alpha$ -MnO<sub>2</sub> [4]. However, after a decade of research, alternative mechanisms have been proposed. A comprehensive review categorizes

these mechanisms as follows [5]: exclusive  $Zn^{2+}$  (de)intercalation,  $H^+$  conversion,  $Zn^{2+}$  and  $H^+$  dual-ion (de)intercalation, mixed intercalation–conversion, deposition–dissolution coupled with (de)intercalation, and exclusive deposition–dissolution. Hybrid reaction mechanisms involving deposition–dissolution and (de)intercalation are also summarized in ref [6]. These conflicting explanations arise partly from the diverse crystal phases of manganese oxides [7] and partly from misattributing XRD peaks of parasitic layered hydroxide products (e.g., zinc basic sulfate,  $Zn_4(OH)_6(SO_4)\cdot nH_2O$  [ZBS] in  $ZnSO_4$  electrolytes) to electrochemically active phases such as zinc buserite, zinc birnessite,  $ZnMn_2O_4$ ,  $MnOOH$ ,  $Mn_2O_3$ ,  $MnO$ , or  $Mn_3O_4$  [5]. For instance, non-operando measurements of discharged  $MnO_2$  cathodes may inadvertently lose intercalated water molecules, complicating the analysis [8,9].

To introduce the deposition–dissolution mechanism, which is the main mechanism for this review, key studies are examined here. In ref. [10], STEM imaging of discharged  $\alpha$ - $MnO_2$  nanowires in 1 M  $ZnSO_4$  (Figure 1b) revealed severe tunnel distortion near the surface, indicative of  $H^+$  intercalation, while the  $2 \times 2$  tunnels showed no occupancy by heavy cations like  $Zn^{2+}$ . EDS mapping further confirmed the absence of Zn in the discharged nanowires. Similarly, ref. [11] demonstrated no Zn incorporation in  $\alpha$ - $MnO_2$  nanowires cycled in 2 M  $ZnSO_4 + 0.1$  M  $MnSO_4$  via EDS (Figure 1c). This suggests  $Zn^{2+}$  intercalation may require  $MnO_2$  phases with larger structural channels, such as  $3 \times 3$  todorokite, layered, or amorphous phases. Notably, both studies observed nanowire fragmentation (Figure 1d) and Zn-rich nanograin formation [10,11], implying  $Zn^{2+}$  (de)intercalation could occur in secondary manganese oxides formed during cycling. Additionally, significant  $Mn^{2+}$  concentration fluctuations during charge/discharge [11–14] support the widely accepted deposition–dissolution mechanism of manganese oxides (with or without  $Mn^{2+}$ ). For example, Zn//ZBS batteries utilizing  $ZnSO_4$ -based electrolytes with varying concentrations of  $MnSO_4$  have been demonstrated (Figure 1e) [15,16]. These findings suggest that the dominant electrochemical process depends critically on electrolyte conditions. The key factors may be the solubility and remaining concentration of  $Mn^{2+}$  in the electrolytes during cycling. For flow batteries, when electrolyte volume exceeds the  $MnO_2$  deposition requirement during charging, excess volume promotes  $MnO_2$  dissolution and stabilizes pH, favoring an exclusive deposition–dissolution mechanism [17]. Furthermore, the formation of inactive materials (e.g.,  $ZnMn_2O_4$ ) in static batteries during cycling, which consume  $Mn^{2+}$ , may also alter reaction pathways, as shown in Figure 1f [18].

Unlike conventional mildly acidic Zn– $MnO_2$  batteries, which rely on  $Mn^{4+}/Mn^{3+}$  redox (theoretical capacity: 308 mAh/g), recent zinc electrolytic  $MnO_2$  batteries utilize a two-electron  $Mn^{2+}/Mn^{4+}$  redox process (theoretical capacity: 616 mAh/g) [19]. These systems also exhibit higher discharge voltages [20]. The remainder of this paper focuses on reviewing advances in cathode-free zinc electrolytic  $MnO_2$  batteries, where  $MnO_2$  is electrochemically deposited onto carbon current collectors from  $Mn^{2+}$ -containing electrolytes [21]. The reactions are summarized in Section 2.2. Without special notes, ions other than  $Zn^{2+}$  and  $Mn^{2+}$  can be regarded as supporting materials.

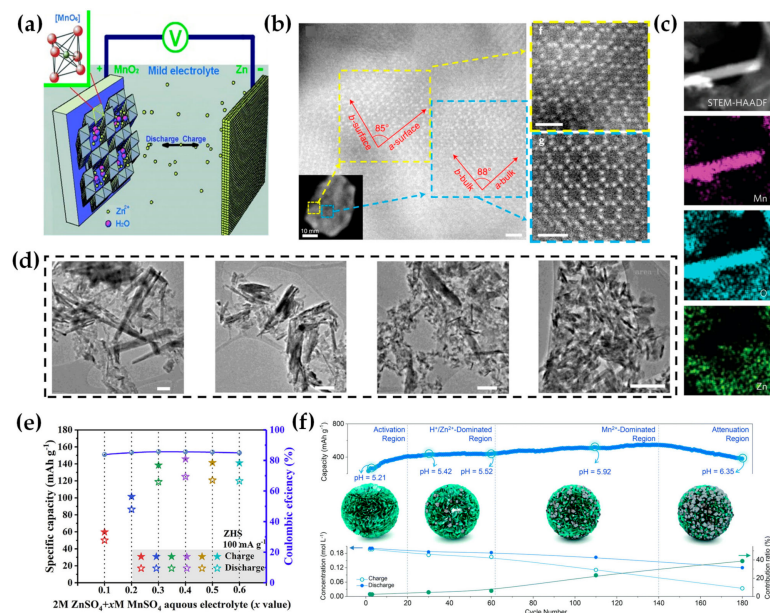


**Figure 1.** The deposition–dissolution mechanism of MnO<sub>2</sub> in zinc-manganese batteries: (a) the first report on a Zn //  $\alpha$ -MnO<sub>2</sub> battery with mild aqueous ZnSO<sub>4</sub> as electrolyte, where Zn<sup>2+</sup> was proposed to insert into the 2 × 2 tunnel structure of  $\alpha$ -MnO<sub>2</sub>. Reproduced with permission from ref. [4]. Copyright 2012, John Wiley & Son; (b) STEM analysis of discharged  $\alpha$ -MnO<sub>2</sub> nanowires. The (001) projections of MnO<sub>2</sub> demonstrate essentially “empty” tunnels without the presence of heavy cations. The high-magnification image (**right**) depicts non-uniform and anisotropic tunnel distortion caused by H<sup>+</sup> intercalation. Reproduced with permission from ref. [10]. Copyright 2022, Springer Nature; (c) STEM-HAADF image of short nanorods and STEM-EDS mappings showing the elemental distributions of Mn, O, and Zn in the MnO<sub>2</sub> electrode during the first discharge cycle. Reproduced with permission from ref. [11]. Copyright 2016, Springer Nature; (d) low-magnification TEM images of the  $\alpha$ -MnO<sub>2</sub> electrode after 1, 10, and 50 cycles (from (**left**) to (**right**)), showing fragmentation during cycling. Reproduced with permission from ref. [10]. Copyright 2022, Springer Nature; (e) charge/discharge capacity and Coulombic efficiency of batteries based on cathode Zn<sub>4</sub>SO<sub>4</sub>(OH)<sub>6</sub>·4H<sub>2</sub>O (ZHS) with 2 M ZnSO<sub>4</sub> + x M MnSO<sub>4</sub> (variable x) electrolytes in the first cycle, where the ZHS serves as electrolyte salts. Reproduced with permission from ref. [15]. Copyright 2020, Elsevier; (f) Mn-based competitive capacity evolution protocol, where the initial MnO<sub>2</sub> is layered structure and the Mn<sup>2+</sup> concentration decreased during cycling. Different mechanism stages are shown at the (**upper**) section along with the cycle profile partitioning and pH values at 1.85 V; the (**middle**) section illustrates micro-mechanism schematics across four regions; the (**bottom**) section presents the Mn<sup>2+</sup> concentration and contribution ratio. Reproduced with permission from ref. [18]. Copyright 2022, Royal Society of Chemistry.

## 2. Electrolytes Modifications

### 2.1. Acid Electrolytes

Since Mn<sup>2+</sup>/MnO<sub>2</sub> redox reactions are more favorable in acidic electrolytes, zinc metal anodes were initially deemed unsuitable for electrolytic MnO<sub>2</sub> batteries due to hydrogen evolution issues [22,23]. Early studies instead explored alternative anodes such as hydrogen (H<sub>2</sub>) [24], Cu [22,23,25], Bi [22], Cd [23] and Pb [26]. For example, the MnO<sub>2</sub>–H<sub>2</sub> battery utilized a 40% platinum-on-carbon catalyst to facilitate H<sub>2</sub> reactions and employed a cylindrical structure for H<sub>2</sub> storage (Figure 2a) [24]. While this system maintained a stable potential of ~1.254 V after 80 h of self-discharge, its remaining capacity was only ~71%. Metals stable in acidic electrolytes (e.g., Cu or Bi) were paired with MnO<sub>2</sub>, achieving open-circuit voltages below 1.2 V (Figure 2b) [22]. However, prolonged cycling revealed Cu<sup>2+</sup> insertion into MnO<sub>2</sub> at discharge voltages < 0.5 V. Then, hybrid systems integrating MnO<sub>2</sub>–Cu and MnO<sub>2</sub>–H<sub>2</sub> via a two-step process were proposed, though at

the cost of Cu consumption,  $\text{H}_2\text{SO}_4$  usage, and excess energy input [25]. Alternatively, toxic Pb- and Cd-based  $\text{MnO}_2$  batteries achieved higher discharge voltages of 1.55 V and 1.68 V, respectively [23,26]. Notably, the  $\text{MnO}_2/\text{Mn}^{2+}$  redox exhibited superior reversibility compared to commercial  $\text{PbO}_2$  cathodes, with higher current density and lower oxygen evolution overpotential (Figure 2c) [26].

The first Zn//electrolytic  $\text{MnO}_2$  battery demonstrated a high discharge voltage of 1.95 V, exceeding those of  $\text{Zn}^{2+}$  or  $\text{H}^+$  insertion mechanisms [20]. This system employed Zn foil, carbon cloth, and an electrolyte of 1 M  $\text{ZnSO}_4$  + 1 M  $\text{MnSO}_4$  + 0.1 M  $\text{H}_2\text{SO}_4$ . Initial charging deposited Zn and  $\varepsilon\text{-MnO}_2$ , while subsequent cycles involved  $\text{H}^+$  and  $\text{Zn}^{2+}$  interactions (Figure 2d) [20]. Remarkably, the low-pH (~1) electrolyte maintained a stable pH and a 2.41 V working window for at least 50 cycles. Later studies showed that adding 0.07 mM polyvinylpyrrolidone (PVP) to this electrolyte significantly improved Coulombic efficiency and cyclability by modulating cationic solvation structures, enhancing  $\text{Mn}^{2+}/\text{Zn}^{2+}$  migration and  $\text{MnO}_2/\text{Zn}$  deposition–dissolution kinetics (Figure 3a) [27].

Beyond  $\text{H}_2\text{SO}_4$ , other acids such as HCl [28], acetic acid (HAc) [29–31] and methanesulfonic acid (MSA) [32] have been explored. Replacing 0.1 M  $\text{H}_2\text{SO}_4$  with 0.2 M HAc in 1 M  $\text{ZnSO}_4$  + 1 M  $\text{MnSO}_4$  increased capacity contributions from (de)intercalation mechanisms (Figure 3b). HAc also reduced anode corrosion and hydrogen evolution while stabilizing pH fluctuations via reversible ionization (Figure 3c), leading to higher reversible capacity and improved cycling stability [29]. The pH buffering effect of HAc is due its weak acid nature compared with  $\text{H}_2\text{SO}_4$  [19], which may be the case for MSA. Comparative studies of Zn// $\alpha\text{-MnO}_2$  batteries in 2 M  $\text{ZnSO}_4$  with 0.1 M  $\text{MnSO}_4$  or carboxylate additives highlighted the buffering effect of anions on interfacial  $\text{H}^+$  and steric hindrance of  $\text{Mn}^{2+}$  migration (Figure 3d) [33]. This mechanism may extend to cathode-free systems. Moreover, further increasing acetate content (e.g., 1 M  $\text{ZnSO}_4$  + 0.1 M  $\text{MnSO}_4$  + 0.1 M NaAc + 0.5 M HAc) shifted the dominant mechanism toward  $\text{MnO}_2$  deposition–dissolution by impeding  $\text{H}^+/\text{Zn}^{2+}$  intercalation [30]. Further modification includes replacing sulfate with acetate and addition of KBr, which tripled ionic conductivity, likely due to  $\text{Br}^-$  integration into  $\text{Zn}^{2+}/\text{Mn}^{2+}$  solvation shells, enhancing cation mobility [31]. In addition, charging protocols also impact performance; while high-voltage constant charging enables fast charging, it promotes  $\text{Mn}^{3+}$  formation, lowering Coulombic efficiency and cycle life (Figure 3e) [32].

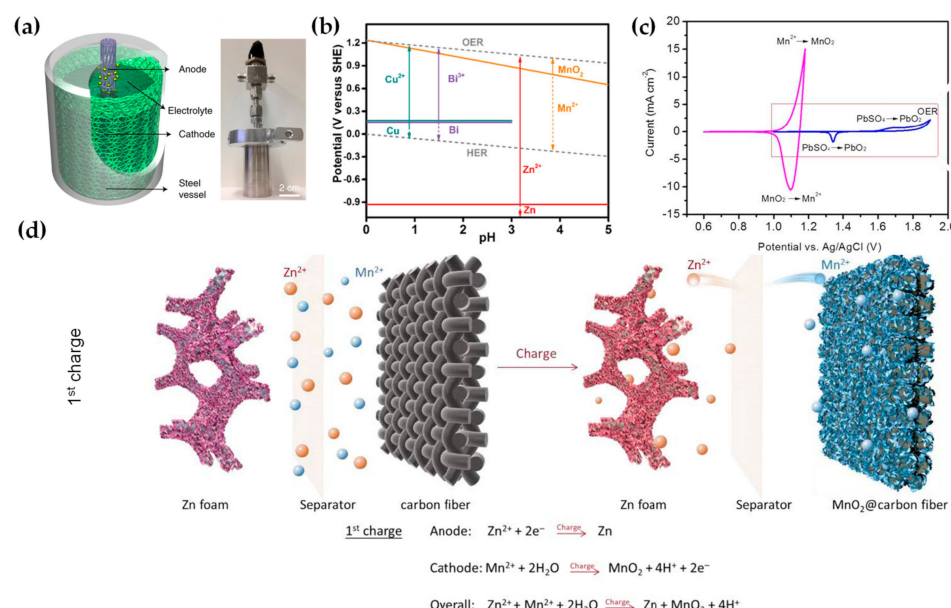


**Figure 2. Cont.**

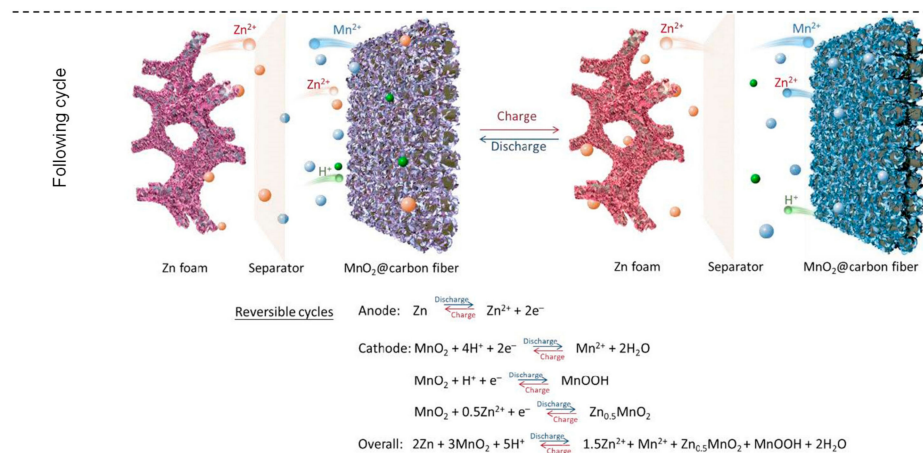


**Figure 2.** Reaction mechanisms of  $Mn^{2+}/MnO_2$  in acidic electrolytes: (a) schematic and digital photograph of the scaled-up membrane-free cylindrical  $Mn-H_2$  cell. Reproduced with permission from ref. [24]. Copyright 2018, Springer Nature; (b) pourbaix diagram of  $MnO_2$  cathode and  $Zn/Bi/Cu$  anode materials under varying pH conditions, to show the voltage difference. Reproduced with permission from ref. [22]. Copyright 2019, John Wiley & Son; (c) cyclic voltammetry (CV) comparison between  $Mn^{2+}/MnO_2$  and  $PbSO_4/PbO_2$  systems, where the currents indicate the reactivity. Reproduced with permission from ref. [26]. Copyright 2020, Royal Society of Chemistry; (d) schematic illustration of reactions steps for the zinc electrolytic  $MnO_2$  battery. Reproduced with permission from ref. [20]. Copyright 2019, John Wiley & Son: (top): Initial chronoamperometric charge process.  $Zn^{2+}$  and  $Mn^{2+}$  cations in the electrolyte are deposited onto the anode and cathode current collectors, forming metallic  $Zn$  and  $MnO_2$ , respectively. (bottom): Subsequent reversible galvanostatic discharge and chronoamperometric charge cycles. During discharge, electrolytic  $MnO_2$  undergoes  $H^+$  and  $Zn^{2+}$  intercalation at the cathode, while  $Zn$  stripping and dissolution occur at the anode.

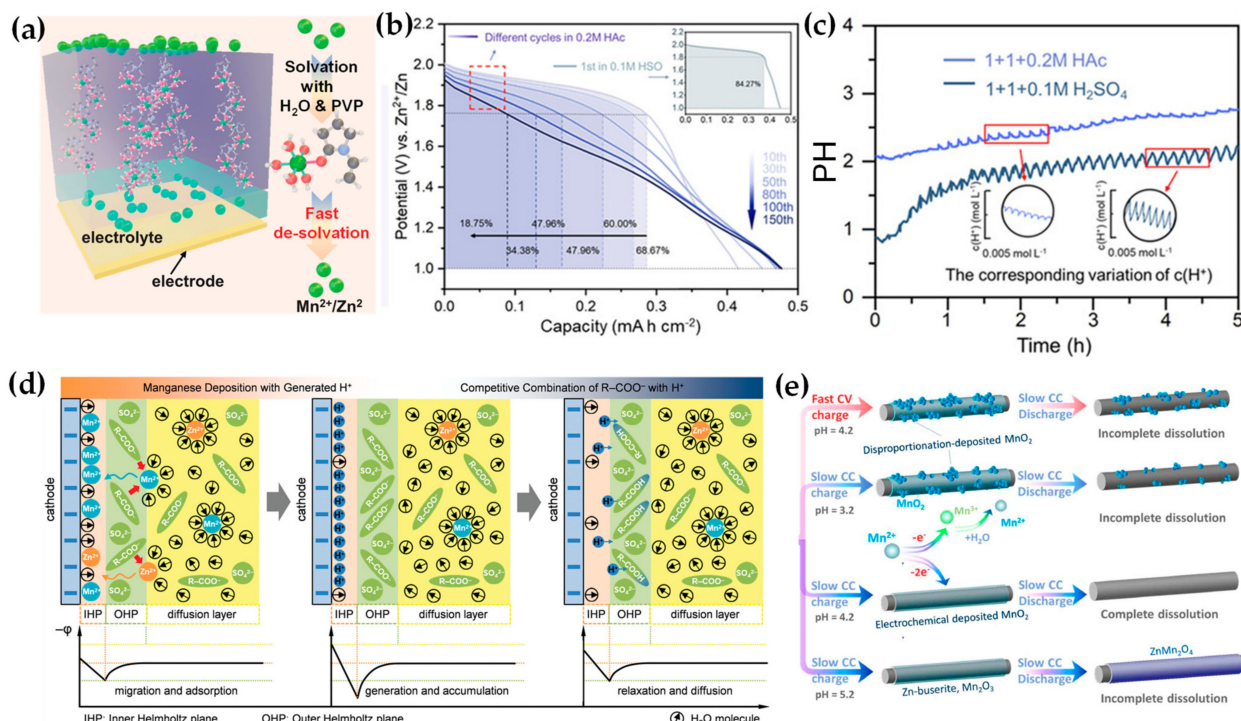


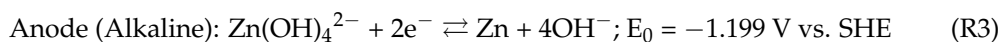
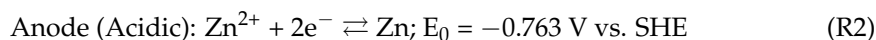
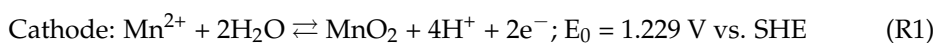
**Figure 3.** Modifications for depositing  $MnO_2$  in acidic electrolytes: (a) schematic of the role of the cationic accelerator (PVP) in facilitating cation transport within aqueous  $MnO_2-Zn$  batteries. Reproduced with permission from ref. [27]. Copyright 2022, John Wiley & Son; (b) galvanostatic discharge profiles and capacity contributions from  $MnO_2$  dissolution in electrolytes containing 0.1 M  $H_2SO_4$  and 0.2 M  $HAc$ , where the high-voltage regions correspond deposition–dissolution process;

(c) *in situ* pH measurements and corresponding H<sup>+</sup> concentrations (circles) during cycling in a battery with 0.1 M HAc and 0.2 M H<sub>2</sub>SO<sub>4</sub>, where less pH fluctuation was showed for HAc case Reproduced with permission from ref. [29]. Copyright 2021, John Wiley & Son; (d) evolution of the electric double layer model at the cathode–electrolyte interface during charging: Modulation of interfacial H<sup>+</sup> concentration and operating potential to thermodynamically enhance capacity. Reproduced with permission from ref. [33]. Copyright 2022, John Wiley & Son. (e) The effects of different charging conditions on the deposited MnO<sub>2</sub>. Reproduced with permission from ref. [32]. Copyright 2023, Elsevier.

## 2.2. Dual Electrolytes

To mitigate Zn corrosion in acidic electrolytes, one strategy involves employing selective membranes and introducing a Zn-compatible secondary electrolyte [34,35]. Unlike the reactions in Figure 2d, the overall cell reaction shifts from Equations (R1) and (R2) to Equations (R1) and (R3), increasing the theoretical potential from 1.992 V to 2.428 V (Figure 4a).

Reactions:



Bipolar membranes (BPMs) were used to separate dual electrolytes, showing lower charge–discharge voltage gaps compared to anion/cation exchange membranes [36]. While BPMs allow H<sup>+</sup>/OH<sup>−</sup> crossover to form water (Figure 4b) [36], another report adopts K<sup>+</sup> and SO<sub>4</sub><sup>2−</sup> permeation [37]. Both systems achieved average voltages of ~2.44 V. Notably, introducing Ni<sup>2+</sup> into the catholyte enhanced Mn<sup>2+</sup>/MnO<sub>2</sub> electrolysis kinetics, improving the high-current (50 C) performance [36].

To prevent electrolyte neutralization, a neutral middle chamber separated by anion/cation exchange membranes was implemented (Figure 4c) [38]. Concentration gradients across the membranes generated an electric field, boosting the open-circuit voltage further to 2.83 V [38]. In this report, a scaled-up static pack powering LED panels using hybrid wind–photovoltaic energy was demonstrated. Similarly, a flow battery variant employed Bi<sub>2</sub>O<sub>3</sub>-modified carbon felt cathodes and Ni<sup>2+</sup>/Mg<sup>2+</sup> catalysts in the catholyte was reported [39]. During charging process, Bi<sub>2</sub>O<sub>3</sub> was dissolved and then reconstructed as nanosized crystal onto MnO<sub>2</sub>, while NiO<sub>2</sub> formed from Ni<sup>2+</sup>. However, despite stable catholyte/anolyte pH, the middle chamber’s pH dropped from 4.8 to 2.35 after five cycles, indicating proton leakage [39].

For systems accepting discharge voltages of ~1.9 V, a membrane with solely anion or cation exchange functions were investigated. For instance, near-neutral anolytes (instead of alkaline) paired with anion exchange membranes (AEMs) were tested (Figure 4d) [40]. To protect the Zn anode from the leaked proton, ZnAc<sub>2</sub> was applied at anolyte to trap the leaked protons [40]. To further shield the proton leakage, hydrophobic bis(trifluoromethylsulfonyl)imide (TFSI<sup>−</sup>)-conducting membranes (PILG: polymer/ionic liquid/graphene) which selectively transported TFSI<sup>−</sup> was applied [41]. However, both anolyte and catholyte required costly TFSI<sup>−</sup> incorporation. As another case, a cation exchange membrane was applied to separate alkaline anolyte and mild acid catholyte; however, the MnO<sub>2</sub> was pre-coated on the cathode first, which may be the reason for its inefficiency of MnO<sub>2</sub> deposition in the mild acid environment [42].

Besides ion-exchange membranes, hydrogels and salt bridges were investigated to separate the dual electrolytes. As shown in Figure 4e, a Zn–MnO<sub>2</sub> battery based on a liquid

acidic catholyte coupled with KOH hydrogel and cellophane as a separator displayed an open-circuit voltage of 2.4–2.8 V [43]. Another cathode-free battery design, shown in Figure 4f, utilized a polyacrylamide (PAM)-based catholyte containing 1 M  $\text{MnSO}_4$  and 1 M  $\text{H}_2\text{SO}_4$ , along with an anolyte of 2 M  $\text{ZnSO}_4$  [44]. Furthermore, a tri-layer hydrogel electrolyte was reported, comprising an acidic region ( $\text{PAM} + \text{ZnSO}_4 + \text{H}^+$ ), a buffer region (sodium polyacrylate ( $\text{PAANa}$ ) +  $\text{ZnSO}_4$ ), and a conservation region ( $\text{PAM} + \text{ZnSO}_4$ ), as illustrated in Figure 4g [45]. Although this approach avoided the use of expensive ion-selective membranes, concerns regarding proton leakage persisted.

When a traditional salt bridge gel composed of  $\text{Na}_2\text{SO}_4$  and agar was employed to separate the alkaline anolyte and acidic catholyte, a discharge voltage of 2.37 V was achieved, as depicted in Figure 4h [46]. For alternative salt bridge strategies, poly(vinyl alcohol) (PVA) gel was first immersed in  $\text{ZnAc}_2$  solution and then in concentrated  $\text{ZnSO}_4$  solution, leveraging strong Hofmeister effects to form a stable salt bridge interface (Figure 4i) [47]. Another study exploited the low solubility of  $\text{K}_2\text{SO}_4$  in Pluronic F-127 (polyethylene–polypropylene glycol). When  $\text{H}_2\text{SO}_4$  catholyte and KOH anolyte came into contact, a self-forming  $\text{K}_2\text{SO}_4$  salt bridge was generated at the interface [48].

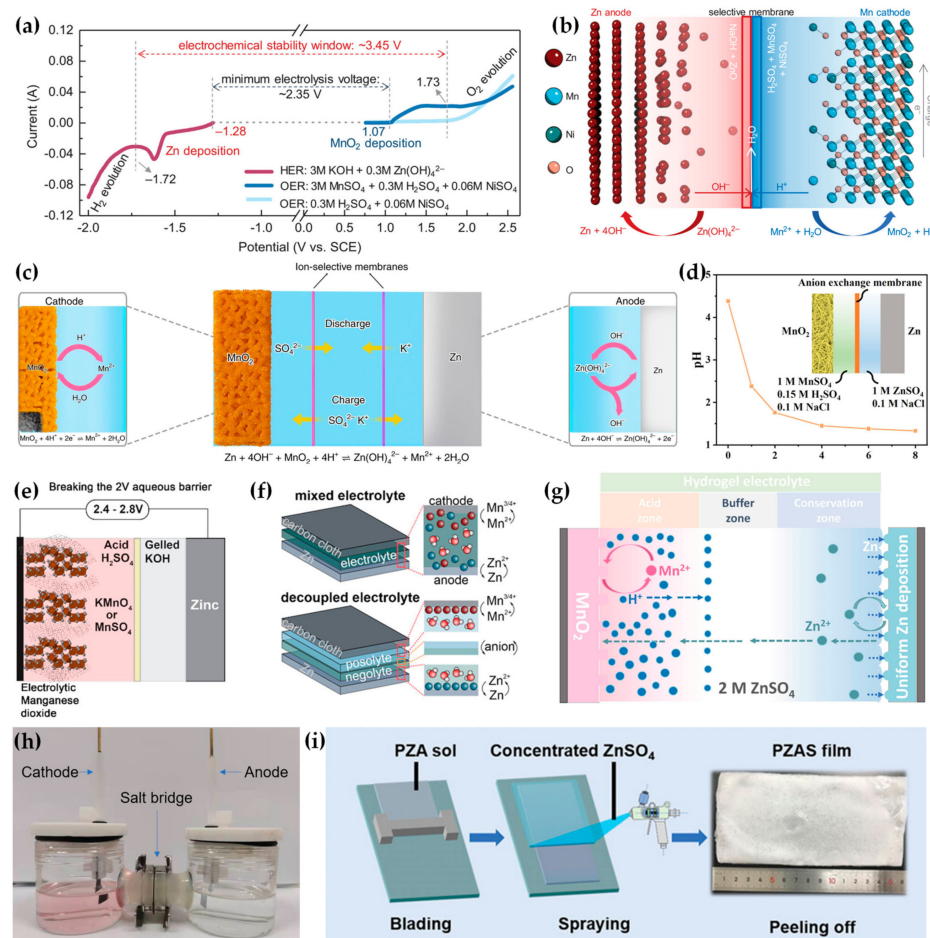


**Figure 4.** Battery configurations with dual electrolytes: (a) electrochemical stability window of the hybrid aqueous battery system and minimum electrolysis voltage required for stable operation; (b) schematic of a  $\text{Zn}/\text{MnO}_2$  hybrid aqueous battery employing dual electrolytes during charge/discharge cycles, where water is formed and decomposed within membranes. Reproduced with permission from ref. [36]. Copyright 2020, John Wiley & Son; (c) cell structure and reaction mechanisms in an aqueous decoupled  $\text{Zn}/\text{MnO}_2$  battery: Acidic and alkaline electrolytes (separated by a neutral central chamber) enable decoupled cathode and anode reactions during discharge/charge. Reproduced with permission from ref. [38]. Copyright 2020, Springer Nature; (d) pH evolution of the

anolyte in an electrolyte-decoupled  $\text{MnO}_2/\text{Zn}$  battery (i.e., acid + neutral electrolytes). Reproduced with permission from ref. [40]. Copyright 2022, American Chemical Society; (e) battery design utilizing alkaline KOH gel electrolyte paired with acidic liquid electrolyte. Reproduced with permission from ref. [43]. Copyright 2019, American Chemical Society; (f) schematic of a cathode-free battery integrating mixed and decoupled gel electrolytes. Reproduced with permission from ref. [44]. Copyright 2021, American Chemical Society; (g) tri-layer hydrogel electrolyte structure in a  $\text{Zn}/\text{MnO}_2$  battery, comprising “Acid zone”, “Buffer zone”, and “Conservation zone”. Reproduced with permission from ref. [45]. Copyright 2021, John Wiley & Son; (h) digital image of a electrolytes-decoupled glass electrolytic cell with a salt bridge. Reproduced with permission from ref. [46]. Copyright 2023, Elsevier; (i) fabrication of PVA-based salt bridge film via the Hofmeister effect. PZA sol denotes a light-white sol after addition of  $\text{ZnAc}_2$  (zinc acetate) to the PVA solution. PZAS gel denotes the PZA sol after addition of concentrated  $\text{ZnSO}_4$  which induces gelation. Reproduced with permission from ref. [47]. Copyright 2022, John Wiley & Son.

### 2.3. Near Neutral Electrolytes

To eliminate the need for ion-selective membranes, near-neutral electrolytes have been investigated for depositing  $\text{MnO}_2$  while mitigating severe Zn anode corrosion. As illustrated in Figure 5a, a membrane-free flow battery was constructed using zinc foil and carbon felt electrodes with a 1 M  $\text{MnSO}_4$  + 1 M  $\text{ZnSO}_4$  electrolyte [17]. Additionally, another novel cell design further enhanced electrolyte utilization by rotating deposited  $\text{MnO}_2$  out of the electrolyte. A subsequent study revealed the detailed experimental parameters, including carbon current collector selection, electrolyte salt concentration/ratio, electrolyte volume, and battery configuration [49]. The results demonstrated that lower  $\text{Zn}^{2+}$  proportions improved discharge curve stability, while higher  $\text{Mn}^{2+}$  concentrations reduced pH (2~4) and elevated discharge voltage. However, excessively high  $\text{Mn}^{2+}$  concentrations (3 M) hindered  $\text{MnO}_2$  dissolution and induced salt precipitation, impairing long-term cycling performance [49].

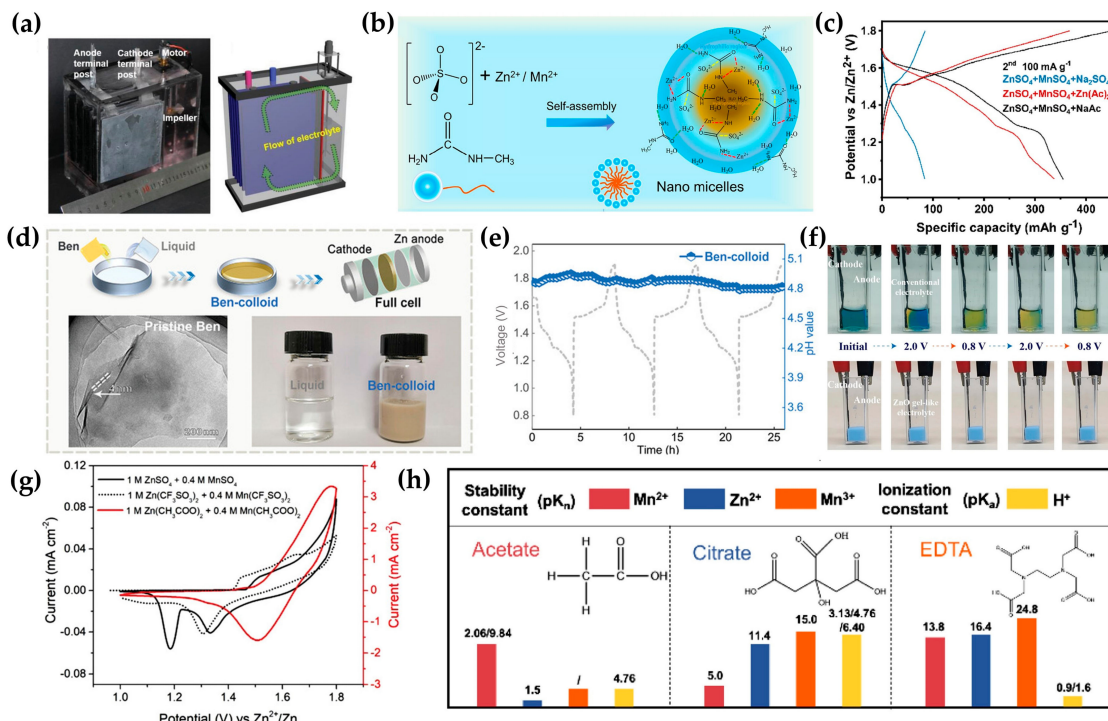


**Figure 5.** Strategies to enhance  $\text{MnO}_2$  deposition in near-neutral electrolytes: (a) digital photograph and cross-sectional schematic of the novel-structured flow cell, with green arrows indicating the electrolyte flow driven by an impeller. Reproduced with permission from ref. [17]. Copyright 2020,

John Wiley & Son; (b) self-assembly of a nanomicelle electrolyte for both Zn plating and MnO<sub>2</sub> deposition within the nanomicelle system. Reproduced with permission from ref. [50]. Copyright 2023, American Chemical Society; (c) specific capacity comparison of Zn//MnO<sub>2</sub> batteries in electrolytes with/without Ac<sup>-</sup> or Na<sup>+</sup>. Reproduced with permission from ref. [51]. Copyright 2022, Elsevier; (d) synthesis of bentonite-colloid (Ben-colloid) electrolyte: (left)—TEM images of pristine bentonite, (right)—Ben-colloid electrolyte versus liquid electrolyte; (e) in situ pH measurements of Zn//MnO<sub>2</sub> batteries cycled with the Ben-colloid electrolyte in a cuvette cell. Reproduced with permission from ref. [52]. Copyright 2022, John Wiley & Son; (f) transparent cuvette cells with a ZnSO<sub>4</sub> + MnSO<sub>4</sub> aqueous electrolyte and a ZnO gel-like electrolyte at different charge/discharge states. Bromocresol green (pH indicator, sensitive range 3.8–5.5) was added to indicate pH. Reproduced with permission from ref. [53]. Copyright 2024, Springer Nature; (g) CV curves illustrating MnO<sub>2</sub> cathode behavior in aqueous electrolytes with different anions. Reproduced with permission from ref. [54]. Copyright 2020, John Wiley & Son; (h) stability constants and ionization constants of complexes formed with acetate, citrate and EDTA. Reproduced with permission from ref. [55]. Copyright 2022, Elsevier.

To enhance the cycling stability of a cathode-free battery (control electrolyte: 0.5 M MnSO<sub>4</sub> + 1 M ZnSO<sub>4</sub>), 7 M methylurea (Mu) was introduced. Mu, containing hydrophilic and hydrophobic moieties, transformed the electrolyte into a nanomicellar system (Figure 5b). These nanomicelles disrupted the continuous aqueous phase and its hydrogen-bonding network, restructuring local hydrogen bonds within micelles or at micelle–water interfaces. Additionally, Mu participated in Zn<sup>2+</sup>/Mn<sup>2+</sup> solvation, displacing water molecules to lower desolvation energy barriers and regulate nanograin formation [50]. The restructured hydrogen-bonding network suppressed water decomposition and parasitic side reactions on the Zn anode. A protective solid–electrolyte interface (SEI) layer ( $Zn_x(Mu)_\gamma SO_4 \cdot nH_2O$ ) also formed, preventing anode corrosion. While the enlarged Zn<sup>2+</sup> solvation radius ( $[Zn(Mu)_x(H_2O)_\gamma]^{2+}$ ) may hinder Zn<sup>2+</sup> intercalation, the elevated pH (5.26) still favored MnO<sub>2</sub> deposition [50]. In another report, glycine (Gly) was explored as an additive for 0.1 M MnSO<sub>4</sub> + 1 M ZnSO<sub>4</sub> electrolyte [56]. Gly complexes with Mn<sup>2+</sup>, releasing H<sup>+</sup> to promote MnO<sub>2</sub> dissolution at the cathode, while adsorbing on the Zn anode surface to shield it from detrimental reactions [56].

The cathode-free battery can also serve as a control sample for normal batteries where MnO<sub>2</sub> is pre-coated on the cathode. For example, the addition of acetate additives to sulfate electrolytes significantly increased the battery capacity, as shown in Figure 5c. This enhanced capacity was validated using stainless steel as the cathode-free electrode, confirming the additional involvement of a dissolution–deposition mechanism [51]. Another example involves the incorporation of bentonite colloid (Ben-colloid) into the electrolyte (Figure 5d). The Ben colloid was hypothesized to self-concentrate Mn<sup>2+</sup> ions and reduce the deposition potential, where a stainless steel was also applied as the cathode-free electrode [52]. Both studies demonstrated the pH buffering effect of these additives with weak acid nature, as illustrated in Figure 5e. Specifically, when excess 0.2 g/mL ZnO was introduced, a gel-like electrolyte formed, maintaining a stable pH of 6.4 throughout the charge–discharge cycles (Figure 5f) [53]. In this gel electrolyte, H<sup>+</sup> ions were effectively eliminated, thereby promoting manganese deposition. Further analysis revealed that Mn<sup>2+</sup> ions and ZBS synergistically generated Zn<sub>2</sub>Mn<sub>3</sub>O<sub>8</sub>·H<sub>2</sub>O nanorod arrays as active material during charging [53]. In a separate study, ZnO was incorporated onto electrodes, but its primary effect appeared to be limited to modifying the electrolyte's pH [57]. Additionally, Mn(H<sub>2</sub>PO<sub>4</sub>)<sub>2</sub> was employed as a pH buffering agent in chloride-based electrolytes [58]. The buffering mechanism for Mn<sup>2+</sup>/MnO<sub>2</sub> conversion was further extended to weak Brønsted acids [59]. Without pH buffering additives, the chloride electrolyte was compared with other anion salts, where 3 M ZnCl<sub>2</sub> + 0.1 M MnCl<sub>2</sub> was recommended [60].

Acetate-based (Ac) electrolytes have been extensively studied. Cyclic voltammetry (CV) of acetate-, sulfate-, and sulfonate-based electrolytes (1 M Zn<sup>2+</sup> + 0.4 M Mn<sup>2+</sup>,

Figure 5g) revealed distinct reaction mechanisms: acetate electrolytes exhibited a two-electron  $\text{MnO}_2/\text{Mn}^{2+}$  reaction (reduction peak at 1.5 V), whereas sulfate/sulfonate systems showed  $\text{Zn}^{2+}/\text{H}^+$  insertion into the  $\text{MnO}_2$  cathode, characterized by dual reduction peaks at 1.35 V and 1.2 V [54]. Complete  $\text{MnO}_2$  dissolution after discharge was confirmed in acetate electrolytes. Density functional theory (DFT) calculations indicated that acetate anions adsorb onto  $\text{MnO}_2$  surface sites, weakening  $\text{H}_2\text{O}$  binding and reducing dissolution energy barriers [54]. Thus, acetate anions enhanced Zn anode compatibility. A flow battery utilizing 0.5 M  $\text{MnAc}_2$  + 0.5 M  $\text{ZnCl}_2$  + 2 M KCl as electrolyte achieved an area capacity of 10 mAh/cm<sup>2</sup> [61]. After applying carbon black coating and higher electrolyte concentrations, the capacity further increased to 20 mAh/cm<sup>2</sup>. Subsequent optimization of electrolyte to 1 M  $\text{MnAc}_2$  + 1 M  $\text{ZnAc}_2$  + 2 M KCl fully coordinated generated  $\text{H}^+$ , achieving an energy density of 42 Wh/L in static batteries [61]. Although  $\text{Mn}^{3+}$  disproportionation was not detected with  $\text{Na}_4\text{P}_2\text{O}_7$  as an indicator, ethylenediaminetetraacetate (EDTA) confirmed  $\text{Mn}^{3+}$  presence due to its stronger complexation capability than  $\text{Ac}^-$  [55,61]. Citrate and EDTA were further compared with acetate as complexing agents (Figure 5h). However, citrate electrolytes exhibited lower pH, while EDTA-based batteries suffered from self-discharge [55]. The criteria for selecting optimal complexing agents were proposed as follows [55]: (i) strong  $\text{Mn}^{2+}$  binding affinity to limit free  $\text{Mn}^{2+}$  concentration; (ii) minimal  $\text{H}^+$  consumption to maintain higher reaction potentials; (iii) weak interactions with  $\text{Zn}^{2+}$  and  $\text{Mn}^{3+}$  to avoid competitive binding ( $\text{Zn}^{2+}$  vs.  $\text{Mn}^{2+}$ ) or  $\text{MnO}_2$  suspension ( $\text{Mn}^{3+}$ -induced instability), thereby preserving Coulombic efficiency (CE).

#### 2.4. Mediator Additives

The disproportionation reaction of oxidized  $\text{Mn}^{3+}$  ( $2\text{Mn}^{3+} + 2\text{H}_2\text{O} \rightarrow \text{MnO}_2 + 4\text{H}^+ + \text{Mn}^{2+}$ ) leads to the formation of “dead”  $\text{MnO}_2$ , which detaches from current collectors [32,55,61,62]. To recycle the dead  $\text{MnO}_2$ , mediator additives are introduced into the electrolyte to reduce it back to  $\text{Mn}^{2+}$ . As shown in Figure 6a,b, the addition of iodide ( $\text{I}^-$ ) enables the oxidation of iodide to  $\text{I}_3^-$ , facilitating the conversion of solid  $\text{MnO}_2$  into soluble  $\text{Mn}^{2+}$  [63]. Figure 6c demonstrates that dead  $\text{MnO}_2$  dispersing in the electrolyte after 18 cycles and can be dissolved completely upon adding KI, resulting in a transparent solution. Moreover, the generated  $\text{I}_3^-$  is also found to contribute to capacity as zinc-iodine batteries [63–65]. Similarly, bromide ( $\text{Br}^-$ ) is proved to enhance capacity (Figure 6d), but its oxidation requires a high charging voltage (e.g., 2.2 V as the case in acidic sulfate electrolytes) [66]. When the charging voltage is fixed below 1.8 V, no  $\text{Br}_2$  forms, and  $\text{Br}^-$  primarily functions to improve electrolyte ion conductivity [31,65]. When chromium cations ( $\text{Cr}^{3+}$ , with  $\text{Cr}^{2+}/\text{Cr}^{3+}$  redox potential at  $-0.407$  V vs. SHE, higher than  $\text{Zn}/\text{Zn}^{2+}$  at  $-0.763$  V vs. SHE) act as mediators, uniform  $\text{MnO}_2$  deposition is promoted (Figure 6e) [55]. Additionally, ultrasonic treatment was proposed to recover batteries by dislodging over-thick  $\text{MnO}_2$  layers (Figure 6f) [55].

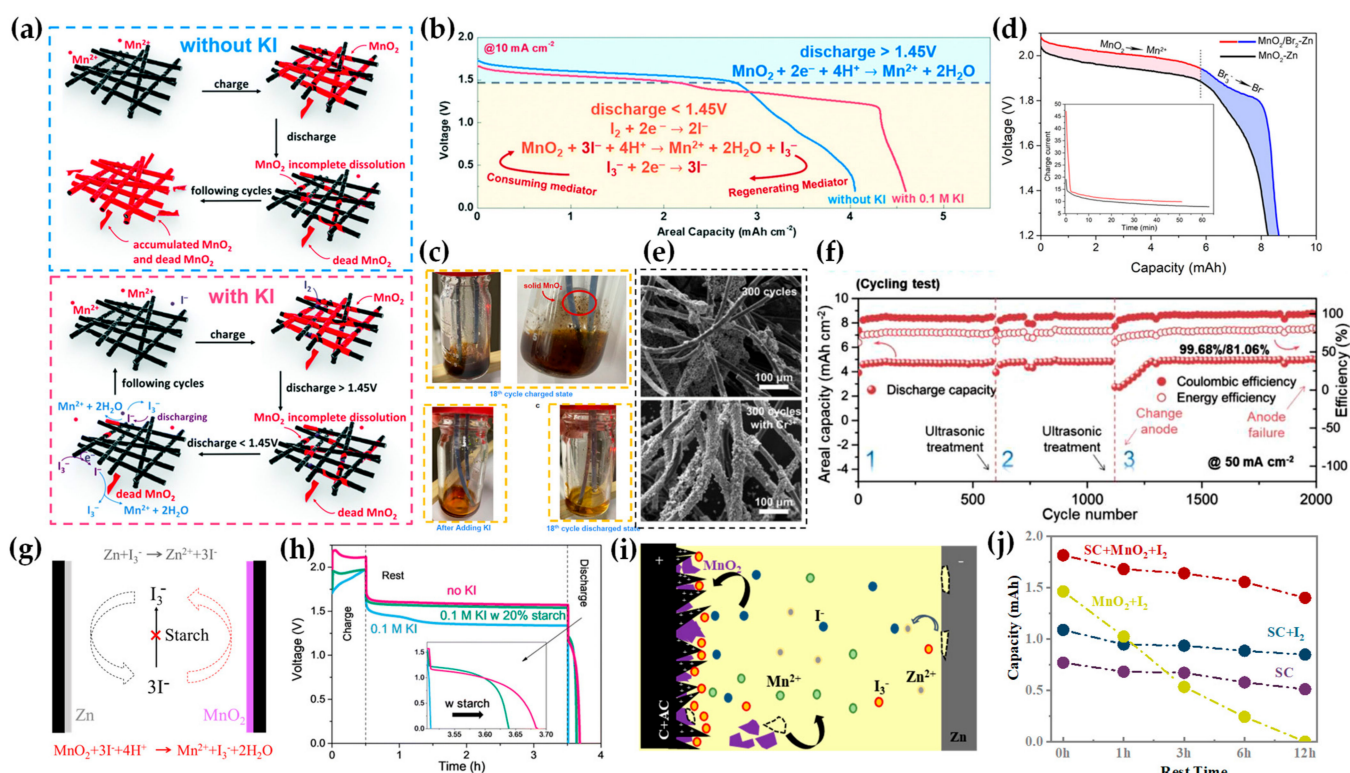


**Figure 6.** Effects of mediator additives—advantages (enhanced capacity and recovery of inactive MnO<sub>2</sub>) and disadvantages (shuttle reactions): (a) schematic comparison of manganese cathodes with/without KI during cycling; (b) discharge profiles of Zn-Mn<sup>2+</sup>/MnO<sub>2</sub> cells with/without 0.1 M KI at the 10th cycle (electrolyte: 1 M MnAc<sub>2</sub> + 1 M ZnAc<sub>2</sub> + 2 M KCl); (c) (top)—optical images of electrolyte before KI addition, (bottom)—electrolyte after KI addition and post-discharge. Reproduced with permission from ref. [63]. Copyright 2022, Royal Society of Chemistry; (d) discharge curves of Zn//MnO<sub>2</sub> batteries after adding Br<sup>-</sup>, with insets showing charge current-time profiles. The additional contribution of the Zn//Br<sub>2</sub> chemical pathway is outlined. Reproduced with permission from ref. [66]. Copyright 2021, American Chemical Society; (e) SEM images indicate more uniform deposition of MnO<sub>2</sub> on carbon fiber after adding Cr<sup>3+</sup> into electrolyte at the 300th cycle; (f) cycling performance of cathode-free Zn//MnO<sub>2</sub> batteries with ultrasonic treatment. Reproduced with permission from ref. [55]. Copyright 2022, Elsevier; (g) shuttle reaction mechanism of I<sup>-</sup>/I<sub>3</sub><sup>-</sup> mediators between Zn and MnO<sub>2</sub>; (h) shelf life of thin-film carbon//carbon batteries with electrolytes containing no KI, 0.1 M KI, or 0.1 M KI + 20% starch. Reproduced with permission from ref. [21]. Copyright 2024, Royal Society of Chemistry; (i) shuttle reactions in the “integrated” devices (supercapacitor + Zn/I<sub>2</sub> battery + Zn//MnO<sub>2</sub> battery) using activated carbon electrodes; (j) shelf-life comparison of hybrid devices: supercapacitor + Zn/I<sub>2</sub> + Zn//MnO<sub>2</sub> (SC + MnO<sub>2</sub> + I<sub>2</sub>), Zn//I<sub>2</sub> + Zn//MnO<sub>2</sub> (MnO<sub>2</sub> + I<sub>2</sub>), supercapacitor + Zn/I<sub>2</sub> (SC + I<sub>2</sub>), and standalone supercapacitor (SC). Self-discharging was checked by remaining capacities after different rest time. Reproduced with permission from ref. [67]. Copyright 2024, Elsevier.

Although mediator additives improve capacity and MnO<sub>2</sub> recovery, they also induce shuttle reactions with both electrodes [21,67,68]. These reactions become severe in thin-film batteries with limited electrolyte volume and narrow electrode gaps (Figure 6g). To mitigate this, starch was added to coordinate with I<sub>3</sub><sup>-</sup>, significantly extending battery shelf life (Figure 6h) [21,68]. Another strategy to mitigate shuttling employs activated carbon electrodes [67]. Compared to graphite, activated carbon’s high surface area provides more sites for MnO<sub>2</sub> anchoring. Furthermore, positive charges accumulating at the cathode (supercapacitor-like effect) electrostatically attract I<sub>3</sub><sup>-</sup>. Combined with reduced MnO<sub>2</sub> detachment and electrostatic interactions, this approach enhances both Coulombic efficiency and shelf life (Figure 6i,j) [67].

### 3. Electrode Modifications

#### 3.1. Anode Modifications

For Zn anodes, constructing a solid electrolyte interface (SEI) is a common strategy to combat hydrogen evolution corrosion (HEC) caused by acidic electrolytes. A proton-resistant Pb-containing interface (composed of Pb and  $\text{Pb}(\text{OH})_2$ ) was formed on Zn anodes (denoted as Zn@Pb) via a facile displacement reaction (i.e., immersing Zn foil in  $\text{PbAc}_2$  solution). This interface further transformed in situ into  $\text{PbSO}_4$  upon  $\text{H}_2\text{SO}_4$  corrosion [69]. When  $\text{PbAc}_2$  was further added to the working electrolyte, Zn anode stability was significantly enhanced (Figure 7a,b). In situ XRD analysis revealed that Pb is plated and stripped on the anode surface during cycling. The Pb layer protects the Zn plating layer from HEC throughout the plating/stripping process due to Pb's low affinity for  $\text{H}^+$  and strong Pb-Zn/Pb-Pb bonding [69].

In another report, a phytic acid (PA)-modified layer was fabricated by soaking Zn foil in a 1% PA solution [70]. Instead of  $\text{H}_2\text{SO}_4$ ,  $\text{H}_3\text{PO}_4$  was used as an acidic additive in the electrolyte. As shown in Figure 7c,d, incorporating  $\text{H}_3\text{PO}_4$  suppressed hydrogen evolution, with an optimal electrolyte pH of 2.2. However, even with the PA-modified layer, HEC occurred when  $\text{H}_2\text{SO}_4$  was introduced [70]. This occurred because zinc phosphate formation at the interface is necessary. During the Zn stripping,  $\text{Zn}^{2+}$  ions accumulate at the interface to form zinc phosphate ( $\text{Zn}_3(\text{PO}_4)_2 \cdot 4\text{H}_2\text{O}$ , ZPO) and zinc hydroxide sulfate ( $\text{Zn}_4\text{SO}_4(\text{OH})_6 \cdot 5\text{H}_2\text{O}$ , ZHS) at the PA-modified layer. Subsequently, during Zn plating,  $\text{H}^+$  ions migrate alongside  $\text{Zn}^{2+}$  to the anode, where they are adsorbed by the PA-modified layer and absorbed by ZPO/ZHS. Throughout repeated plating/stripping cycles,  $\text{H}^+$  ions are reversibly adsorbed within the interphase, maintaining a stable proton concentration in the electrolyte [70].

#### 3.2. Cathode Modifications

For most studied pre-coated  $\text{MnO}_2$  batteries, constructing a cathode electrolyte interface (CEI) is a common strategy to suppress  $\text{MnO}_2$  dissolution. Here, the CEI layer prevents dead  $\text{MnO}_2$  dispersion into the electrolyte via limiting  $\text{Mn}^{2+}$  diffusion. However, though we need the CEI to capture  $\text{Mn}^{3+}$  and  $\text{H}^+$ , the CEI layer must also allow  $\text{MnO}_2/\text{Mn}^{2+}$  redox reactions, as illustrated in Figure 7e [71]. After evaluating the electrostatic potential distributions of monomers, including acrylamide (AAm), 2-acrylamido-2-methylpropanesulfonic acid (AMPS), 2-chloroacrylic acid (ClAA), acrylic acid (AA), methacrylic acid (MAA), and vinylphosphonic acid (VPA), MAA was selected for in situ gel polymerization on carbon cloth (PMAA@CC) in the presence of  $\text{Zn}^{2+}$  and  $\text{Mn}^{2+}$  [71]. By minimizing dead  $\text{MnO}_2$  in the electrolyte,  $\text{H}^+$  generation is reduced, which in turn mitigates Zn anode corrosion and enhancing the reversibility of  $\text{MnO}_2/\text{Mn}^{2+}$  reactions. Another approach to suppress  $\text{Mn}^{3+}$  diffusion and disproportionation involves manganese polyacrylate (PAAMn), which was coated on stainless steel foil as a cathode active material [72]. Due to the relatively low ion conductivity, the diffusion of  $\text{Mn}^{3+}$  may also be limited in hydrogels, as reported in refs. [44,45,73,74].

Doping deposited  $\text{MnO}_2$  is an effective method to improve conductivity. In dual-electrolyte systems,  $\text{Ni}^{3+}$  and  $\text{Bi}^{3+}$  doping catalyzes  $\text{Mn}^{2+}/\text{MnO}_2$  reactions and enhances  $\text{MnO}_2$  conductivity without concerns about cation crossover due to anolyte/catholyte separation [36,39,75]. For single-electrolyte batteries, bismuth (III) pyridine-3,5-dicarboxylate (BiMOF) was employed as a  $\text{Bi}^{3+}$  reservoir to stabilize  $\text{MnO}_2$  structure by controlled  $\text{Bi}^{3+}$  release during  $\text{Mn}^{2+}$  deposition [76]. Similarly, adding  $\text{Al}^{3+}$  to the electrolyte was reported to form a proton–donor reservoir to maintain acidic conditions and to introduce oxygen vacancies into  $\text{MnO}_2$  [77].

As different phases were reported for the deposited  $\text{MnO}_2$ , the crystal structure may vary with factors, such as anions, pH, and charging protocols. Notably, incorporating 0.1 mM surfactant molecules into the electrolyte induces favorable c-axis orientation in hexagonal Zn and  $\text{MnO}_2$  deposition (Figure 7f) [78]. The surfactant (e.g., t-Oct-C<sub>6</sub>H<sub>4</sub>- $(\text{OCH}_2\text{CH}_2)_n\text{OH}$ ,  $n \approx 9\text{--}10$ ) with hydrophobic tail and hydrophilic head first form an aligned bilayer structure, followed by a gradient liquid crystal interphase during deposition. This interphase comprises lamellar liquid crystals (near the electrode), hexagonal liquid crystals (intermediate), and micelle clusters (near the electrolyte). Consequently, the layered  $\delta$ -phase  $\text{MnO}_2$  was deposited instead of the  $\epsilon$ -phase. (Figure 7g). Additionally, the surfactant promotes (002) plane growth of Zn, yielding a flat, compact anode morphology with enhanced corrosion resistance against hydrogen evolution [78].

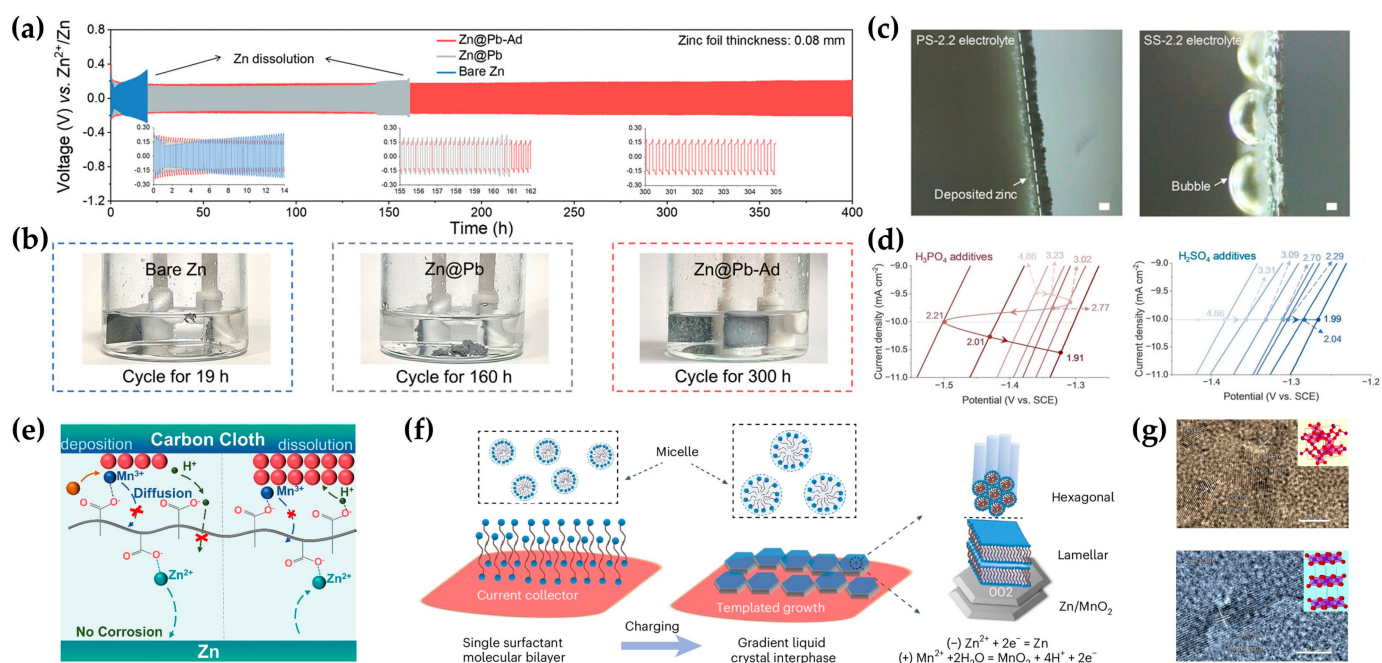


**Figure 7.** Anti-corrosion strategies for Zn anodes and modifications to mitigate dissolution and crystal structures of  $\text{MnO}_2$  cathode: (a) cycling performance of  $\text{Zn@Pb-Ad}$  ( $\text{Ad}$  denotes  $\text{PbAc}_2$  additive in electrolyte),  $\text{Zn@Pb}$ , and bare Zn symmetric batteries in 0.2 M  $\text{H}_2\text{SO}_4$  ( $4 \text{ mA cm}^{-2}$ ,  $0.5 \text{ mAh cm}^{-2}$ ); (b) post-cycling photographs of Zn symmetric batteries, where the control bare Zn anode fell apart. Reproduced with permission from ref. [69]. Copyright 2023, John Wiley & Son; (c) optical images of Zn deposition on PAZn anodes with  $\text{H}_3\text{PO}_4$  (PS) or  $\text{H}_2\text{SO}_4$  (SS) additives at  $30 \text{ mA cm}^{-2}$  for 6 min. Hydrogen bubble formed for the  $\text{H}_2\text{SO}_4$  case; (d) linear sweep voltammetry (LSV) curves of PAZn anodes in 1 M  $\text{Na}_2\text{SO}_4$  at varying pH adjusted by  $\text{H}_3\text{PO}_4/\text{H}_2\text{SO}_4$ . The S shape curve for the  $\text{H}_3\text{PO}_4$  case indicates the existence of optimal pH value. Reproduced with permission from ref. [70]. Copyright 2025, John Wiley & Son; (e) in situ hydrogel ion-anchoring strategy to form CEI for suppressing  $\text{Mn}^{3+}$  and  $\text{H}^+$  diffusion. Reproduced with permission from ref. [71]. Copyright 2024, American Chemical Society; (f) dynamic phase transition during deposition: from aligned surfactant bilayers to gradient liquid crystal interphases (lamellar near the electrode, hexagonal intermediate, and micelle clusters near the electrolyte); (g) TEM images of  $\text{MnO}_2$  deposited in pristine electrolyte ( $\epsilon$ -phase, (top)) versus surfactant-modified electrolyte ( $\delta$ -phase, (bottom)). Reproduced with permission from ref. [78]. Copyright 2024, Springer Nature.

### 3.3. Current Collectors

For the cathode-free structure, the initial charging process deposits  $\text{MnO}_2$  from the electrolyte onto current collectors. During this step, metallic zinc is also plated, suggesting that a conventional zinc foil anode may be unnecessary. A dual electrode-free structure—

using current collectors as initial electrodes—was demonstrated in  $\text{MnO}_2\text{-Cd}/\text{Zn/Cu}$  batteries (Figure 8a) [21,23,78,79]. Furthermore, the cycling performance of cuvette cells and thin-film batteries with/without zinc anodes was compared using an electrolyte containing  $1 \text{ M ZnAc}_2 + 1 \text{ M MnAc}_2 + 2 \text{ M KCl} + 0.1 \text{ M KI}$ . Results showed that electrode-free thin-film batteries (carbon//carbon configuration) exhibited lower Coulombic efficiencies (CEs) but longer cycle life than Zn//carbon systems (Figure 8b) [21]. Thus, although excess zinc compensates for deposition inefficiency and corrosion losses, it intensifies hydrogen evolution side reactions. Hydrogen generation caused battery inflation and failure, particularly sensitive in sealed thin-film structures with lean electrolyte volume and confined space, which are closer to real-world applications [21].

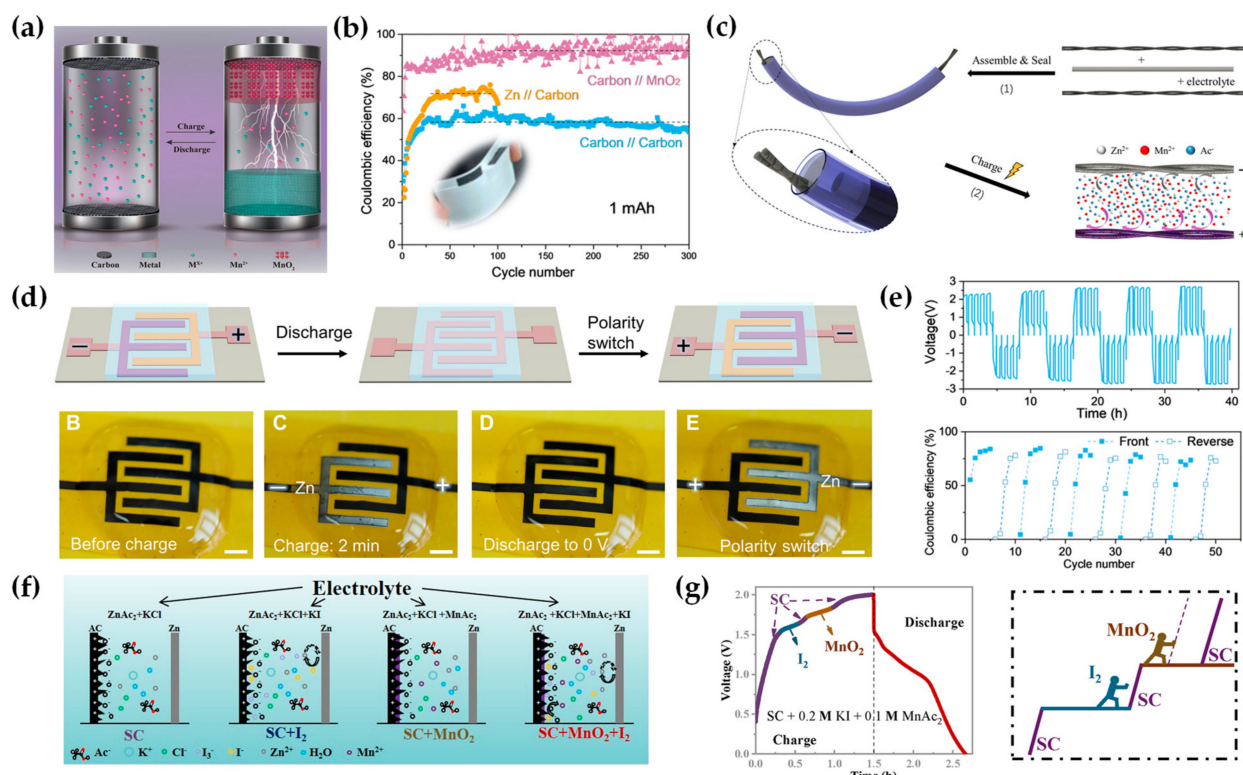


**Figure 8.** Dual electrode-free devices and integrated systems combining supercapacitors with batteries: (a) schematic of an electrode-free  $\text{Zn}/\text{MnO}_2$  battery structure Reproduced with permission from ref. [23]. Copyright 2021, John Wiley & Son; (b) cycling performance of thin-film batteries with carbon//carbon,  $\text{Zn}/\text{carbon}$ , and carbon// $\text{MnO}_2$  electrodes, which proved the unnecessary of pre-coated anode.; (c) fabrication process and structural design of cable-type batteries, which demonstrates dual electrode-free configuration for fiber battery. Reproduced with permission from ref. [21]. Copyright 2024, Royal Society of Chemistry; (d) polarity-switchable  $\text{Zn}/\text{Br}_2$  microbattery with in operando visualization, which demonstrates electrode-free configuration for microbattery. The switchable polarity also applies for another case based on  $0.5 \text{ M MnAc}_2 + 0.5 \text{ M ZnAc}_2$ . Reproduced with permission from ref. [79]. Copyright 2022, the American Association for the Advancement of Science; (e) voltage profiles and Coulombic efficiencies (CEs) of cuvette graphite felt//graphite felt batteries showing electrode polarity reversed every 5 cycles, which shows the adaptation of CEs under switched polarities. Reproduced with permission from ref. [21]. Copyright 2024, Royal Society of Chemistry; (f) electrolyte design strategy enabling integrated zinc battery-supercapacitor functionalities; (g) stepwise charging mechanism of hybrid devices. As the voltage platform can be regulated by  $\text{KI}$  and  $\text{MnAc}_2$  concentrations, a typical shaped charge/discharge curve is illustrated. Reproduced with permission from ref. [67]. Copyright 2024, Elsevier.

Interestingly, the electrode-free design enables a facile assembly of batteries with complex geometries. For example, a cable-shaped battery was fabricated by embedding two

commercial carbon fiber ropes in a starch gel electrolyte (Figure 8c) [21,68]. During initial charging, Zn and MnO<sub>2</sub> were directly deposited on the fibers, eliminating troublesome pre-coating steps. Here, the starch additive not only stabilized the gel electrolyte but also suppressed iodide-mediated shuttle reactions [21,68]. Another example is a micro-battery (Figure 8c), where polyacrylamide (PAM) hydrogel was applied to microelectrodes [79]. After full discharge, the battery reverts to its initial state (only current collectors), enabling polarity switching (Figure 8d,e). This feature enhances safety during over-discharge and expands application flexibility [21,79].

Integrating supercapacitor electrodes with the electrolyte of a zinc electrolytic MnO<sub>2</sub> battery yielded a hybrid “supercapattery” (Figure 8f) [67]. For conventional supercapacitors, the stored charge quantity Q is only proportional to charged voltage V, if the capacitance C is fixed, i.e.,  $Q = C \times V$ . However, the electrochemical working window of the aqueous electrolytes is limited by the water decomposition. Thus, we integrated the two types of devices by leveraging Zn–I<sub>2</sub> and Zn–MnO<sub>2</sub> charge/discharge platforms, circumventing water decomposition limits. Furthermore, the iodide additive can recover dead MnO<sub>2</sub>. Overall, a flexible thin-film device that combines supercapacitor, Zn–I<sub>2</sub> and Zn–MnO<sub>2</sub> functionalities was demonstrated (Figure 8g). This integration outperformed individual components in capacity, shelf life, and cycle stability [67].

#### 4. Outlooks and Perspectives

To reveal detailed information about the reviewed battery structures, Table 1 lists the electrode materials and electrolyte formulations. By categorizing recent strategies for performance and stability enhancement into electrolyte and electrode modifications, we propose the following possible research directions:

**Table 1.** Reported cathode-free zinc electrolytic MnO<sub>2</sub> batteries: anode and cathode materials, electrolyte composition, device structure, and highest area capacities. The additives are marked in bold.

Anode	Cathode	Electrolyte	Device Structure	Capacity (mAh/cm <sup>2</sup> )	Ref.
Pt/C	Carbon felt	1 M MnSO <sub>4</sub> + 0.05 M H <sub>2</sub> SO <sub>4</sub>	Swagelok cell Cylindrical cell	4 2	[24]
Cu plate Carbon cloth Zn plate	Carbon cloth	0.3 M CuSO <sub>4</sub> + 0.3 M MnSO <sub>4</sub> + 0.5 M H <sub>2</sub> SO <sub>4</sub> 0.1 M Bi(NO <sub>3</sub> ) <sub>3</sub> + 0.1 M MnSO <sub>4</sub> + 1 M HNO <sub>3</sub> 0.3 M ZnSO <sub>4</sub> + 0.3 M MnSO <sub>4</sub>	Pouch cell	0.8	[22]
PbSO <sub>4</sub> /Pb	Carbon felt	0.5 M H <sub>2</sub> SO <sub>4</sub> + 1 M MnSO <sub>4</sub>	Pouch cell Flow cell	24.4 4.88	[26]
Carbon cloth	Carbon cloth	0.5 M CdSO <sub>4</sub> + 0.5 M MnSO <sub>4</sub> + 0.5 M H <sub>2</sub> SO <sub>4</sub> 0.5 M CuSO <sub>4</sub> + 0.5 M MnSO <sub>4</sub> + 0.5 M H <sub>2</sub> SO <sub>4</sub> 1 M ZnSO <sub>4</sub> + 1 M MnSO <sub>4</sub> + 0.1 M H <sub>2</sub> SO <sub>4</sub>	Home-made cell	10 0.5 0.5	[23]
Zn foam	Carbon cloth	1 M ZnSO <sub>4</sub> + 1 M MnSO <sub>4</sub> + 0.1 M H <sub>2</sub> SO <sub>4</sub>	Home-made cell	10	[20]
Zn foil	Carbon felt	1 M ZnSO <sub>4</sub> + 1 M MnSO <sub>4</sub> + 0.1 M H <sub>2</sub> SO <sub>4</sub> + 0.07 mM polvinylpyrrolidone (PVP)	Beaker cell	4	[27]
Zn foil	Carbon felt	1 M ZnCl <sub>2</sub> + 1 M MnCl <sub>2</sub> + 0.2 M HCl	Home-made cell	0.5	[28]
Zn foil	Carbon felt	1 M ZnSO <sub>4</sub> + 1 M MnSO <sub>4</sub> + 0.2 M HAc	Pouch cell	2	[29]
Zn foil	Carbon felt	1 M ZnAc <sub>2</sub> + 0.5 M HAc + 0.5 M MnAc <sub>2</sub> + 1 M KBr	Beaker cell	17	[31]
Zn plate	Carbon felt	1 M MnAc <sub>2</sub> + 1 M ZnO + 2.5 M MSA + 1 M KCl	Beaker cell	2	[32]
3D porous Zn @carbon-felt	Carbon felt	3 M NaOH + 0.3 M ZnO/bipolar membrane/ 3 M MnSO <sub>4</sub> + 0.3 M H <sub>2</sub> SO <sub>4</sub> + 0.06 M NiSO <sub>4</sub>	Home-made cell	13	[36]
Zn foil	Carbon cloth	2.4 M KOH + 0.1 M ZnAc <sub>2</sub> /bipolar membrane/ 1 M MnSO <sub>4</sub> + 0.5 M H <sub>2</sub> SO <sub>4</sub>	Home-made cell Flow cell	15	[37]
Zn foil	MnO <sub>2</sub> loaded carbon felt	6 M KOH + 0.2 M ZnO + 5 mM vanillin // 0.1 M K <sub>2</sub> SO <sub>4</sub> // 3 M H <sub>2</sub> SO <sub>4</sub> + 0.1 M MnSO <sub>4</sub>	Pack	66.3	[38]
Zn metal on carbon felt	Bi <sub>2</sub> O <sub>3</sub> coated carbon felt	4 M NaOH + 0.1 M ZnO + 5 mM vanillin // 3 M Li <sub>2</sub> SO <sub>4</sub> // 0.1 M MnSO <sub>4</sub> + 2.5 M H <sub>2</sub> SO <sub>4</sub> + 0.03 M NiSO <sub>4</sub> + 0.01 M MgSO <sub>4</sub>	Flow cell	22.6	[39]

**Table 1.** Cont.

Anode	Cathode	Electrolyte	Device Structure	Capacity (mAh/cm <sup>2</sup> )	Ref.
Zn foil	Carbon felt	0.8 M ZnSO <sub>4</sub> + 0.2 M ZnAc <sub>2</sub> + 0.1 M NaCl // 1 M MnSO <sub>4</sub> + 0.15 M H <sub>2</sub> SO <sub>4</sub> + 0.1 M NaCl	Beaker cell	7.3	[40]
Zn foil	Carbon paper	0.5 M ZnSO <sub>4</sub> + 1 M LiTFSI // PILG/1 M MnSO <sub>4</sub> + 1 M HTFSI	Home-made cell	18	[41]
Zn foil	MnO <sub>2</sub> loaded carbon felt	1 M NaOH + 0.01 M ZnAc <sub>2</sub> /Na+-form Nafion membrane/2 M ZnSO <sub>4</sub> + 0.1 M MnSO <sub>4</sub>	Glass cylinders	-	[42]
Zn foil	Carbon cloth	2 M ZnSO <sub>4</sub> in PAM // <sub>1/2</sub> M MnSO <sub>4</sub> + 1 M H <sub>2</sub> SO <sub>4</sub> in PAM	Simple pouch	0.7	[44]
Zn foil	Carbon cloth	3 M KOH + 0.3 M ZnO/NaSO <sub>4</sub> agar // 3 M MnSO <sub>4</sub> + 0.3 M H <sub>2</sub> SO <sub>4</sub>	H-shaped electrolytic cell	1.35	[46]
Zn foil	Carbon felt	1 M ZnSO <sub>4</sub> + 1 M MnSO <sub>4</sub>	Flow cell	2	[17]
Zn foil	Carbon cloth	1 M ZnSO <sub>4</sub> + 2 M MnSO <sub>4</sub>	Beaker cell	2	[49]
Zn foil	Carbon cloth	1 M ZnSO <sub>4</sub> + 0.5 M MnSO <sub>4</sub> + 7 M methylurea	Open thin-film cell	0.5	[50]
Zn foil	Carbon cloth	1 M ZnSO <sub>4</sub> + 0.1 M MnSO <sub>4</sub> + 3 M Glycine	Coin cell	0.5	[56]
Zn foil	Carbon nanotube film	1 M ZnSO <sub>4</sub> + 0.1 M MnSO <sub>4</sub> + 0.2 g/mL ZnO + 0.25 g/mL ZnO	Coin cell Pouch cell	2.5 0.46	[53]
ZnO@C	Carbon cloth	ZnSO <sub>4</sub> +PVA/1 M MnCl <sub>2</sub> + 1 M ZnSO <sub>4</sub> + H <sub>2</sub> SO <sub>4</sub>	-	0.5	[57]
Zn foil	Graphite foil	3 M ZnCl <sub>2</sub> + 0.1 M MnCl <sub>2</sub>	Home-made cell	10	[60]
Zn foil	Carbon cloth	1 M ZnAc <sub>2</sub> + 0.4 M MnAc <sub>2</sub>	Coin cell Swagelok cell	0.5 1	[54]
Zn on graphite felt	Carbon black on graphite	1.5 M MnAc <sub>2</sub> + 1.5 M ZnCl <sub>2</sub> + 3 M KCl	Flow cell	20	[61]
Zn foil	Carbon felt	1 M ZnAc <sub>2</sub> + 1 M MnAc <sub>2</sub> + 2 M KCl + 0.1 M KI	Flow cell	20	[63]
Zn foil	Carbon felt	1 M MnSO <sub>4</sub> + 1 M ZnSO <sub>4</sub> + 0.03 M ZnI <sub>2</sub>	Home-made cell	20	[64]
Zn foil	Carbon felt	0.5 M HAc + 0.5 M MnAc <sub>2</sub> + 1 M ZnAc <sub>2</sub> + 1 M KBr + 0.1 M KI	Home-made cell	20	[65]
Zn foil	Carbon felt	1 M ZnSO <sub>4</sub> + 1 M MnSO <sub>4</sub> + 0.2 M H <sub>2</sub> SO <sub>4</sub> + 0.05 M ZnBr <sub>2</sub> + 0.2 M Br <sub>2</sub>	Home-made cell	13.3	[66]
Zn foil	Carbon cloth Carbon felt	0.5 M ZnCl <sub>2</sub> + 0.5 M MnAc <sub>2</sub> + 2 M KCl + 1.75 M HAc + 0.05 M CrCl <sub>3</sub>	Pouch cell	5	[55]
Printed zinc	Printed graphite	1 M ZnAc <sub>2</sub> + 1 M MnAc <sub>2</sub> + 2 M KCl + 0.1 M KI	Thin-film cell	0.1	[68]
Zn@Pb	Graphite felt	0.2/0.1 M H <sub>2</sub> SO <sub>4</sub> + 1 M ZnSO <sub>4</sub> + 1 M MnSO <sub>4</sub> + PbAc <sub>2</sub>	Home-made cell	5	[69]
Phytic acid modified Zn	Carbon cloth	1 M ZnSO <sub>4</sub> + 0.5 M MnSO <sub>4</sub> + H <sub>3</sub> PO <sub>4</sub>	Pouch cell	10	[70]
Zn foil	PMAA@CC	1 M ZnAc <sub>2</sub> + 0.4 M MnAc <sub>2</sub>	Pouch cell	1	[71]
Zn foil	PAAMn@SS	1 M ZnSO <sub>4</sub> + 0.5 M MnSO <sub>4</sub>	-	0.1	[72]
Zn foil	BiMOF@Carbon paper	1 M ZnSO <sub>4</sub> + 0.2 M MnSO <sub>4</sub>	-	0.17	[76]
Zn foil	Graphite foil	0.25 M Al <sub>2</sub> (SO <sub>4</sub> ) <sub>3</sub> + 2 M ZnSO <sub>4</sub> + 0.5 M MnSO <sub>4</sub>	Home-made cell	2	[77]
Cu foil	Carbon felt	1 M ZnSO <sub>4</sub> + 0.2 M MnSO <sub>4</sub> + 0.1 mM surfactant	Coin cell	3	[78]
Printed graphite	Printed graphite	1 M ZnAc <sub>2</sub> + 1 M MnAc <sub>2</sub> + 2 M KCl + 0.1 M KI	Thin-film cell	0.1	[21]
Printed zinc	Printed activated carbon	1 M ZnAc <sub>2</sub> + 1 M MnAc <sub>2</sub> + 2 M KCl + 0.1 M KI	Thin-film cell	0.5	[67]

**Electrolyte pH:** Although initial electrolytes may be neutral, the charging process will generate H<sup>+</sup>, which inevitably acidifies the electrolyte. This acidic environment accelerates Zn anode corrosion and hydrogen evolution, leading to gas-induced battery inflation.

**Electrolyte Volume:** While electrolytes serve as material sources for Zn // MnO<sub>2</sub> deposition, excessive volumes (taking 30 μL/cm<sup>2</sup> for thin-film battery as a reference) reduce material utilization efficiency. Optimization should balance electrolyte quantity with deposition kinetics.

**Zn Anode:** Despite advances in Zn alloys and SEI layers for widely studied zinc-ion batteries (mostly based on mild acid sulphate electrolytes), their application in electrolytic

$\text{MnO}_2$  systems (mostly based on in acid or acetate electrolytes) remains unexplored. Translating these innovations may mitigate corrosion and hydrogen evolution.

**MnO<sub>2</sub> Cathode:** Industrial electrolytic manganese dioxide (EMD) dominates the primary market. Studying doping and phase transitions during *in situ*  $\text{MnO}_2$  electrodeposition may help to refine EMD production processes.

**Current Collectors:** Excess Zn addition compensates for anode loss but obscures the reaction mechanisms. Single or dual electrode-free configurations are recommended as control experiment samples. Additionally, alignment between real-world application conditions and laboratory battery designs should be considered. For instance, carbon cloth/felt's high surface area differs significantly from printed electrodes, potentially limiting practical relevance.

**Battery Design:** Thin-film batteries with lean electrolytes and compact dimensions closely mimic real-world applications. These structures are highly sensitive to hydrogen accumulation and have been commercialized (e.g., Zinergy's products).

**Shelf Life:** Long-term stability tests are critical, especially for systems employing mediator additives prone to shuttle reactions.

**Integrated Devices:** Activated carbon electrodes enhance  $\text{MnO}_2$  anchoring and contribute pseudocapacitive capacity. Hybrid supercapattery designs (combining supercapacitors with Zn– $\text{MnO}_2/\text{I}_2$  chemistries) offer superior performance and novel mechanistic pathways.

**Author Contributions:** S.L. (Shiwei Liu): Data curation; Visualization; Validation; Software. Z.L.: Methodology; Investigation. H.Z.: Resources, Funding acquisition. W.C.: Methodology. J.W.: Resources. Q.Z.: Methodology. G.Y.: Formal analysis. W.A.D.: Resources. Z.N.: Funding acquisition; Project administration. P.H.: Funding acquisition; Project administration. S.L. (Shiqiang Luo): Conceptualization; Writing—Original draft preparation. G.A.J.A.: Supervision; Writing—Review and Editing. All authors have read and agreed to the published version of the manuscript.

**Funding:** This research was funded by the Guangdong Introducing Innovative and Entrepreneurial Teams Program, grant number 2019ZT08Z656 and by the Shenzhen Science and Technology Program, grant number KJZD20230923113759002, SZXJP20230703093207017 and KQTD20190929172522248.

**Data Availability Statement:** The data presented in this study are available upon request from the corresponding authors.

**Acknowledgments:** This work is supported by the Guangdong Introducing Innovative and Entrepreneurial Teams Program, the Shenzhen Science and Technology Program and the Shenzhen Association for Science and Technology.

**Conflicts of Interest:** Authors Shiwei Liu, Zanxiang Nie, Pritesh Hirralal, Shiqiang Luo and Gehan A. J. Amaratunga were employed by Zinergy Shenzhen Ltd. The remaining authors declare that the research was conducted in the absence of any commercial or financial relationships that could be construed as a potential conflict of interest.

## References

1. Luan, J.; Yuan, H.; Liu, J.; Zhong, C. Recent advances on charge storage mechanisms and optimization strategies of Mn-based cathode in zinc-manganese oxides batteries. *Energy Storage Mater.* **2024**, *66*, 103206. [[CrossRef](#)]
2. Zhang, Z.; Li, W.; Shen, Y.; Wang, R.; Li, H.; Zhou, M.; Wang, W.; Wang, K.; Jiang, K. Issues and opportunities of manganese-based materials for enhanced Zn-ion storage performances. *J. Energy Storage* **2022**, *45*, 103729. [[CrossRef](#)]
3. Shoji, T.; Hishinuma, M.; Yamamoto, T. Zinc-manganese dioxide galvanic cell using zinc sulphate as electrolyte. Rechargeability of the cell. *J. Appl. Electrochem.* **1988**, *18*, 521–526. [[CrossRef](#)]
4. Xu, C.J.; Li, B.H.; Du, H.D.; Kang, F.Y. Energetic Zinc Ion Chemistry: The Rechargeable Zinc Ion Battery. *Angew. Chem. Int. Edit.* **2012**, *51*, 933–935. [[CrossRef](#)]
5. Sambandam, B.; Mathew, V.; Kim, S.; Lee, S.; Kim, S.; Hwang, J.Y.; Fan, H.J.; Kim, J. An analysis of the electrochemical mechanism of manganese oxides in aqueous zinc batteries. *Chem.* **2022**, *8*, 924–946. [[CrossRef](#)]

6. Zhang, N.; Ji, Y.-R.; Wang, J.-C.; Wang, P.-F.; Zhu, Y.-R.; Yi, T.-F. Understanding of the charge storage mechanism of MnO<sub>2</sub>-based aqueous zinc-ion batteries: Reaction processes and regulation strategies. *J. Energy Chem.* **2023**, *82*, 423–463. [[CrossRef](#)]
7. Zhang, N.; Wang, J.C.; Guo, Y.F.; Wang, P.F.; Zhu, Y.R.; Yi, T.F. Insights on rational design and energy storage mechanism of Mn-based cathode materials towards high performance aqueous zinc-ion batteries. *Coordin. Chem. Rev.* **2023**, *479*, 215009. [[CrossRef](#)]
8. Lee, B.; Lee, H.R.; Kim, H.; Chung, K.Y.; Cho, B.W.; Oh, S.H. Elucidating the intercalation mechanism of zinc ions into alpha-MnO<sub>2</sub> for rechargeable zinc batteries. *Chem. Commun.* **2015**, *51*, 9265–9268. [[CrossRef](#)]
9. Chamoun, M.; Brant, W.R.; Tai, C.W.; Karlsson, G.; Noreus, D. Rechargeability of aqueous sulfate Zn/MnO<sub>2</sub> batteries enhanced by accessible Mn<sup>2+</sup> ions. *Energy Storage Mater.* **2018**, *15*, 351–360. [[CrossRef](#)]
10. Yuan, Y.F.; Sharpe, R.; He, K.; Li, C.H.; Saray, M.T.; Liu, T.C.; Yao, W.T.; Cheng, M.; Jin, H.L.; Wang, S.; et al. Understanding intercalation chemistry for sustainable aqueous zinc-manganese dioxide batteries. *Nat. Sustain.* **2022**, *5*, 890–898. [[CrossRef](#)]
11. Pan, H.; Shao, Y.; Yan, P.; Cheng, Y.; Han, K.S.; Nie, Z.; Wang, C.; Yang, J.; Li, X.; Bhattacharya, P.; et al. Reversible aqueous zinc/manganese oxide energy storage from conversion reactions. *Nat. Energy* **2016**, *1*, 16039. [[CrossRef](#)]
12. Kim, S.H.; Oh, S.M. Degradation mechanism of layered MnO<sub>2</sub> cathodes in Zn/ZnSO<sub>4</sub>/MnO<sub>2</sub> rechargeable cells. *J. Power Sources* **1998**, *72*, 150–158. [[CrossRef](#)]
13. Wu, D.R.; Housel, L.M.; Kim, S.J.; Sadique, N.; Quilty, C.D.; Wu, L.J.; Tappero, R.; Nicholas, S.L.; Ehrlich, S.; Zhu, Y.M.; et al. Quantitative temporally and spatially resolved X-ray fluorescence microprobe characterization of the manganese dissolution-deposition mechanism in aqueous Zn/alpha-MnO<sub>2</sub> batteries. *Energ. Environ. Sci.* **2020**, *13*, 4322–4333. [[CrossRef](#)]
14. Moon, H.; Ha, K.H.; Park, Y.; Lee, J.; Kwon, M.S.; Lim, J.; Lee, M.H.; Kim, D.H.; Choi, J.H.; Choi, J.H.; et al. Direct Proof of the Reversible Dissolution/Deposition of Mn<sup>2+</sup>/Mn<sup>4+</sup> for Mild-Acid Zn-MnO<sub>2</sub> Batteries with Porous Carbon Interlayers. *Adv. Sci.* **2021**, *8*, 2003714. [[CrossRef](#)] [[PubMed](#)]
15. Guo, X.; Zhou, J.; Bai, C.L.; Li, X.K.; Fang, G.Z.; Liang, S.Q. Zn/MnO<sub>2</sub> battery chemistry with dissolution-deposition mechanism. *Mater. Today Energy* **2020**, *16*, 100396. [[CrossRef](#)]
16. Chen, H.; Dai, C.L.; Xiao, F.Y.; Yang, Q.J.; Cai, S.N.; Xu, M.W.; Fan, H.J.; Bao, S.J. Reunderstanding the Reaction Mechanism of Aqueous Zn-Mn Batteries with Sulfate Electrolytes: Role of the Zinc Sulfate Hydroxide. *Adv. Mater.* **2022**, *34*, 2109092. [[CrossRef](#)] [[PubMed](#)]
17. Li, G.D.; Chen, W.; Zhang, H.; Gong, Y.J.; Shi, F.F.; Wang, J.Y.; Zhang, R.F.; Chen, G.X.; Jin, Y.; Wu, T.; et al. Membrane-Free Zn/MnO<sub>2</sub> Flow Battery for Large-Scale Energy Storage. *Adv. Energy Mater.* **2020**, *10*, 1902085. [[CrossRef](#)]
18. Yang, H.; Zhou, W.H.; Chen, D.; Liu, J.H.; Yuan, Z.Y.; Lu, M.J.; Shen, L.F.; Shulga, V.; Han, W.; Chao, D.L. The origin of capacity fluctuation and rescue of dead Mn-based Zn-ion batteries: A Mn-based competitive capacity evolution protocol. *Energ. Environ. Sci.* **2021**, *15*, 1106–1118. [[CrossRef](#)]
19. Liu, Z.; Qin, L.; Lu, B.; Wu, X.; Liang, S.; Zhou, J. Issues and Opportunities Facing Aqueous Mn<sup>2+</sup>/MnO<sub>2</sub>-based Batteries. *ChemSusChem* **2022**, *15*, e202200348. [[CrossRef](#)]
20. Chao, D.L.; Zhou, W.H.; Ye, C.; Zhang, Q.H.; Chen, Y.G.; Gu, L.; Davey, K.; Qiao, S.Z. An Electrolytic Zn-MnO<sub>2</sub> Battery for High-Voltage and Scalable Energy Storage. *Angew. Chem. Int. Ed.* **2019**, *58*, 7823–7828. [[CrossRef](#)]
21. Luo, S.; Liu, S.; Yang, G.; Liu, C.; Wu, J.; Hiralal, P.; Nie, Z.; Amaratunga, G.A.J.; Zhou, H. Electrode-free flexible batteries enabled by electro-deposition of both Zn and MnO<sub>2</sub> from electrolytes. *New J. Chem.* **2024**, *48*, 1462–1466. [[CrossRef](#)]
22. Liang, G.; Mo, F.; Li, H.; Tang, Z.; Liu, Z.; Wang, D.; Yang, Q.; Ma, L.; Zhi, C. A Universal Principle to Design Reversible Aqueous Batteries Based on Deposition–Dissolution Mechanism. *Adv. Energy Mater.* **2019**, *9*, 1901838. [[CrossRef](#)]
23. Wang, M.; Chen, N.; Zhu, Z.; Meng, Y.; Shen, C.; Zheng, X.; Liang, D.; Chen, W. Electrode-Less MnO<sub>2</sub>-Metal Batteries with Deposition and Stripping Chemistry. *Small* **2021**, *17*, 2103921. [[CrossRef](#)] [[PubMed](#)]
24. Chen, W.; Li, G.; Pei, A.; Li, Y.; Liao, L.; Wang, H.; Wan, J.; Liang, Z.; Chen, G.; Zhang, H.; et al. A manganese–hydrogen battery with potential for grid-scale energy storage. *Nat. Energy* **2018**, *3*, 428–435. [[CrossRef](#)]
25. Huang, J.; Guo, Z.; Dong, X.; Bin, D.; Wang, Y.; Xia, Y. Low-cost and high safe manganese-based aqueous battery for grid energy storage and conversion. *Sci. Bull.* **2019**, *64*, 1780–1787. [[CrossRef](#)]
26. Huang, J.; Yan, L.; Bin, D.; Dong, X.; Wang, Y.; Xia, Y. An aqueous manganese–lead battery for large-scale energy storage. *J. Mater. Chem. A* **2020**, *8*, 5959–5967. [[CrossRef](#)]
27. Chuai, M.Y.; Yang, J.L.; Tan, R.; Liu, Z.C.; Yuan, Y.; Xu, Y.; Sun, J.F.; Wang, M.M.; Zheng, X.H.; Chen, N.; et al. Theory-Driven Design of a Cationic Accelerator for High-Performance Electrolytic MnO<sub>2</sub>-Zn Batteries. *Adv. Mater.* **2022**, *34*, 2203249. [[CrossRef](#)]
28. Feng, Z.Y.; Gao, Z.Y.; Xue, Z.Y.; Yang, M.; Zhao, X.Y. Acidity Modulation of Electrolyte Enables High Reversible Mn<sup>2+</sup>/MnO<sub>2</sub> Electrode Reaction of Electrolytic Zn-MnO<sub>2</sub> Battery. *J. Electron. Mater.* **2022**, *51*, 6041–6046. [[CrossRef](#)]
29. Liu, Z.X.; Yang, Y.Q.; Liang, S.Q.; Lu, B.A.; Zhou, J. pH-Buffer Contained Electrolyte for Self-Adjusted Cathode-Free Zn-MnO<sub>2</sub> Batteries with Coexistence of Dual Mechanisms. *Small Struct.* **2021**, *2*, 2100119. [[CrossRef](#)]

30. He, Z.F.; Lu, Y.T.; Wei, T.C.; Hu, C.C. Complementary Operando Electrochemical Quartz Crystal Microbalance and UV/Vis Spectroscopic Studies: Acetate Effects on Zinc-Manganese Batteries. *ChemSusChem* **2023**, *16*, e202300259. [CrossRef]
31. Wu, J.; Li, Y.N.; Huang, J.Q.; Chi, X.W.; Yang, J.H.; Liu, Y. Bromide-acetate co-mediated high-power density rechargeable aqueous zinc-manganese dioxide batteries. *J. Mater. Chem. A* **2021**, *9*, 21888–21896. [CrossRef]
32. Wang, H.; Wang, T.; Stevenson, G.; Chamoun, M.; Lindström, R.W. MnO<sub>2</sub>/Mn<sup>2+</sup> chemistry: Charging protocol and electrolyte regulation. *Energy Storage Mater.* **2023**, *63*, 103008. [CrossRef]
33. Liu, Z.; Li, L.; Qin, L.; Guo, S.; Fang, G.; Luo, Z.; Liang, S. Balanced Interfacial Ion Concentration and Migration Steric Hindrance Promoting High-Efficiency Deposition/Dissolution Battery Chemistry. *Adv. Mater.* **2022**, *34*, 2204681. [CrossRef] [PubMed]
34. Durena, R.; Zukuls, A. A Short Review: Comparison of Zinc-Manganese Dioxide Batteries with Different pH Aqueous Electrolytes. *Batteries* **2023**, *9*, 311. [CrossRef]
35. Dai, C.; Hu, L.; Jin, X.; Zhao, Y.; Qu, L. The Emerging of Aqueous Zinc-Based Dual Electrolytic Batteries. *Small* **2021**, *17*, e2008043. [CrossRef] [PubMed]
36. Chao, D.; Ye, C.; Xie, F.; Zhou, W.; Zhang, Q.; Gu, Q.; Davey, K.; Gu, L.; Qiao, S.-Z. Atomic Engineering Catalyzed MnO<sub>2</sub> Electrolysis Kinetics for a Hybrid Aqueous Battery with High Power and Energy Density. *Adv. Mater.* **2020**, *32*, 2001894. [CrossRef]
37. Liu, C.; Chi, X.; Han, Q.; Liu, Y. A High Energy Density Aqueous Battery Achieved by Dual Dissolution/Deposition Reactions Separated in Acid-Alkaline Electrolyte. *Adv. Energy Mater.* **2020**, *10*, 1903589. [CrossRef]
38. Zhong, C.; Liu, B.; Ding, J.; Liu, X.R.; Zhong, Y.W.; Li, Y.; Sun, C.B.; Han, X.P.; Deng, Y.D.; Zhao, N.Q.; et al. Decoupling electrolytes towards stable and high-energy rechargeable aqueous zinc-manganese dioxide batteries. *Nat. Energy* **2020**, *5*, 440–449. [CrossRef]
39. Kim, M.; Lee, S.; Choi, J.; Park, J.; Park, J.W.; Park, M. Reversible metal ionic catalysts for high-voltage aqueous hybrid zinc-manganese redox flow batteries. *Energy Storage Mater.* **2023**, *55*, 698–707. [CrossRef]
40. Sun, J.F.; Liu, Z.C.; Li, K.; Yuan, Y.; Zheng, X.H.; Xu, Y.; Wang, M.M.; Chuai, M.; Hu, H.L.; Chen, W. Proton-Trapping Agent for Mitigating Hydrogen Evolution Corrosion of Zn for an Electrolytic MnO<sub>2</sub>/Zn Battery. *ACS Appl. Mater. Interfaces* **2022**, *14*, 51900–51909. [CrossRef]
41. Cui, Y.F.; Zhuang, Z.B.; Xie, Z.L.; Cao, R.F.; Hao, Q.; Zhang, N.; Liu, W.Q.; Zhu, Y.H.; Huang, G. High-Energy and Long-Lived Zn-MnO<sub>2</sub> Battery Enabled by a Hydrophobic-Ion-Conducting Membrane. *ACS Nano* **2022**, *16*, 20730–20738. [CrossRef] [PubMed]
42. Fan, W.J.; Liu, F.; Liu, Y.; Wu, Z.X.; Wang, L.L.; Zhang, Y.; Huang, Q.H.; Fu, L.J.; Wu, Y.P. A high voltage aqueous zinc-manganese battery using a hybrid alkaline-mild electrolyte. *Chem. Commun.* **2020**, *56*, 2039–2042. [CrossRef] [PubMed]
43. Yadav, G.G.; Turney, D.; Huang, J.C.; Wei, X.; Banerjee, S. Breaking the 2 V Barrier in Aqueous Zinc Chemistry: Creating 2.45 and 2.8 V MnO<sub>2</sub>-Zn Aqueous Batteries. *ACS Energy Lett.* **2019**, *4*, 2144–2146. [CrossRef]
44. Tang, H.; Yin, Y.; Huang, Y.; Wang, J.; Liu, L.; Qu, Z.; Zhang, H.; Li, Y.; Zhu, M.; Schmidt, O.G. Battery-Everywhere Design Based on a Cathodeless Configuration with High Sustainability and Energy Density. *ACS Energy Lett.* **2021**, *6*, 1859–1868. [CrossRef]
45. Shen, Z.X.; Tang, Z.Q.; Li, C.W.; Luo, L.; Pu, J.; Wen, Z.R.; Liu, Y.; Ji, Y.; Xie, J.P.; Wang, L.T.; et al. Precise Proton Redistribution for Two-Electron Redox in Aqueous Zinc/Manganese Dioxide Batteries. *Adv. Energy Mater.* **2021**, *11*, 2102055. [CrossRef]
46. Xu, Q.; Xie, Q.X.; Xue, T.; Cheng, G.; Wu, J.D.; Ning, L.; Yan, X.H.; Lu, Y.J.; Zou, Z.L.; Wang, B.P.; et al. Salt Bridge-intermediated three phase decoupling electrolytes for high voltage electrolytic aqueous Zinc-Manganese dioxides battery. *Chem. Eng. J.* **2023**, *451*, 138775. [CrossRef]
47. Yuan, Y.; Yang, J.L.; Liu, Z.C.; Tan, R.; Chuai, M.; Sun, J.F.; Xu, Y.; Zheng, X.H.; Wang, M.M.; Ahmad, T.; et al. A Proton-Barrier Separator Induced via Hofmeister Effect for High-Performance Electrolytic MnO<sub>2</sub>-Zn Batteries. *Adv. Energy Mater.* **2022**, *12*, 2103705. [CrossRef]
48. Durena, R.; Zukuls, A.; Vanags, M.; Sutka, A. How to increase the potential of aqueous Zn-MnO<sub>2</sub> batteries: The effect of pH gradient electrolyte. *Electrochim. Acta* **2022**, *434*, 141275. [CrossRef]
49. Panda, M.R.; El Meragawi, S.; Mirshekarloo, M.S.; Chen, W.; Shaibani, M.; Majumder, M. Acidity-Aided Surface Modification Strategy to Enhance In Situ MnO<sub>2</sub> Deposition for High Performance Zn-MnO<sub>2</sub> Battery Prototypes. *Small* **2024**, *2311933*. [CrossRef]
50. Deng, Y.; Wang, H.; Fan, M.; Zhan, B.; Zuo, L.-J.; Chen, C.; Yan, L. Nanomicellar Electrolyte to Control Release Ions and Reconstruct Hydrogen Bonding Network for Ultrastable High-Energy-Density Zn-Mn Battery. *J. Am. Chem. Soc.* **2023**, *145*, 20109–20120. [CrossRef]
51. Zhong, Z.P.; Li, J.Y.; Li, L.Y.; Xi, X.Y.; Luo, Z.G.; Fang, G.Z.; Liang, S.Q.; Wang, X.Y. Improving performance of zinc-manganese battery via efficient deposition/dissolution chemistry. *Energy Storage Mater.* **2022**, *46*, 165–174. [CrossRef]
52. Xie, X.; Fu, H.; Fang, Y.; Lu, B.; Zhou, J.; Liang, S. Manipulating Ion Concentration to Boost Two-Electron Mn<sup>4+</sup>/Mn<sup>2+</sup> Redox Kinetics through a Colloid Electrolyte for High-Capacity Zinc Batteries. *Adv. Energy Mater.* **2021**, *12*, 2102393. [CrossRef]
53. Wu, J.; Tang, Y.; Xu, H.; Ma, G.; Jiang, J.; Xian, C.; Xu, M.; Bao, S.-J.; Chen, H. ZnO Additive Boosts Charging Speed and Cycling Stability of Electrolytic Zn–Mn Batteries. *Nano-Micro Lett.* **2024**, *16*, 74. [CrossRef]

54. Zeng, X.H.; Liu, J.T.; Mao, J.F.; Hao, J.N.; Wang, Z.J.; Zhou, S.; Ling, C.D.; Guo, Z.P. Toward a Reversible Mn<sup>4+</sup>/Mn<sup>2+</sup> Redox Reaction and Dendrite-Free Zn Anode in Near-Neutral Aqueous Zn/MnO<sub>2</sub> Batteries via Salt Anion Chemistry. *Adv. Energy Mater.* **2020**, *10*, 1904163. [CrossRef]
55. Liu, Z.X.; Yang, Y.Q.; Lu, B.A.; Liang, S.Q.; Fan, H.J.; Zhou, J. Insights into complexing effects in acetate-based Zn-MnO<sub>2</sub> batteries and performance enhancement by all-round strategies. *Energy Storage Mater.* **2022**, *52*, 104–110. [CrossRef]
56. Kong, M.Z.; Zhang, T.; Bu, H.X.; Li, C.L.; Zhang, X.X.; Zhang, J.; Liu, W.J.; Li, D.Z.; Wang, C.G.; Xu, X.J. Enhancing the efficiency of two-electron zinc-manganese batteries enabled by Glycine complexation of manganese ions and compatibility with zinc anodes. *Chem. Eng. J.* **2024**, *499*, 156426. [CrossRef]
57. Yang, L.; Meng, L.; Ji, X.; Cheng, S. Construction of Zinc-based Anodes for Electrolytic Zinc-MnO<sub>2</sub> Batteries with High Discharge Voltage and Good Durability. *Batter. Supercaps* **2023**, *6*, e202300158. [CrossRef]
58. Liu, Y.Z.; Qin, Z.M.; Yang, X.P.; Liu, J.; Liu, X.X.; Sun, X.Q. High-Voltage Manganese Oxide Cathode with Two-Electron Transfer Enabled by a Phosphate Proton Reservoir for Aqueous Zinc Batteries. *ACS Energy Lett.* **2022**, *7*, 1814–1819. [CrossRef]
59. Mateos, M.; Makivic, N.; Kim, Y.-S.; Limoges, B.; Balland, V. Accessing the Two-Electron Charge Storage Capacity of MnO<sub>2</sub> in Mild Aqueous Electrolytes. *Adv. Energy Mater.* **2020**, *10*, 2000332. [CrossRef]
60. Lv, H.; Song, Y.; Qin, Z.; Zhang, M.; Yang, D.; Pan, Q.; Wang, Z.; Mu, X.; Meng, J.; Sun, X.; et al. Disproportionation enabling reversible MnO<sub>2</sub>/Mn<sup>2+</sup> transformation in a mild aqueous Zn-MnO<sub>2</sub> hybrid battery. *Chem. Eng. J.* **2022**, *430*, 133064. [CrossRef]
61. Xie, C.X.; Li, T.Y.; Deng, C.Z.; Song, Y.; Zhang, H.M.; Li, X.F. A highly reversible neutral zinc/manganese battery for stationary energy storage. *Energ. Environ. Sci.* **2020**, *13*, 135–143. [CrossRef]
62. Ye, X.; Han, D.; Jiang, G.; Cui, C.; Guo, Y.; Wang, Y.; Zhang, Z.; Weng, Z.; Yang, Q.-H. Unraveling the deposition/dissolution chemistry of MnO<sub>2</sub> for high-energy aqueous batteries. *Energ. Environ. Sci.* **2023**, *16*, 1016–1023. [CrossRef]
63. Lei, J.F.; Yao, Y.X.; Wang, Z.Y.; Lu, Y.C. Towards high-areal-capacity aqueous zinc-manganese batteries: Promoting MnO<sub>2</sub> dissolution by redox mediators. *Energ. Environ. Sci.* **2021**, *14*, 4418–4426. [CrossRef]
64. Zheng, X.; Luo, R.; Ahmad, T.; Sun, J.; Liu, S.; Chen, N.; Wang, M.; Yuan, Y.; Chuai, M.; Xu, Y.; et al. Development of High Areal Capacity Electrolytic MnO<sub>2</sub>-Zn Battery via an Iodine Mediator. *Energy Environ. Mater.* **2023**, *6*, e12433. [CrossRef]
65. Wu, J.; Huang, J.Q.; Yang, J.H.; Chi, X.W.; Liu, Y. Mn<sup>2+</sup>/I<sup>-</sup> Hybrid Cathode with Superior Conversion Efficiency for Ultrahigh-Areal-Capacity Aqueous Zinc Batteries. *ACS Appl. Mater. Inter.* **2022**, *14*, 53627–53635. [CrossRef]
66. Zheng, X.H.; Wang, Y.C.; Xu, Y.; Ahmad, T.; Yuan, Y.; Sun, J.F.; Luo, R.H.; Wang, M.M.; Chuai, M.Y.; Chen, N.; et al. Boosting Electrolytic MnO<sub>2</sub>-Zn Batteries by a Bromine Mediator. *Nano Lett.* **2021**, *21*, 8863–8871. [CrossRef]
67. Liu, S.; Luo, S.; Amaratunga, G.A.J.; Hiralal, P.; Nie, Z. Thin-film flexible zinc hybrid electrochemical device integrating three chemical pathways. *J. Power Sources* **2024**, *614*, 235045. [CrossRef]
68. Liu, S.; Hiralal, P.; Nie, Z.; Amaratunga, G.A.J.; Luo, S. Thin-film electrolytic MnO<sub>2</sub>-Zn batteries with limited amount of acetate electrolyte. *Mater. Lett.* **2024**, *357*, 135780. [CrossRef]
69. Ruan, P.; Chen, X.; Qin, L.; Tang, Y.; Lu, B.; Zeng, Z.; Liang, S.; Zhou, J. Achieving Highly Proton-Resistant Zn-Pb Anode through Low Hydrogen Affinity and Strong Bonding for Long-Life Electrolytic Zn//MnO<sub>2</sub> Battery. *Adv. Mater.* **2023**, *35*, e2300577. [CrossRef]
70. Yang, H.; Li, L.; Chen, D.; Wang, J.; Tan, Y.; Jiang, Z.; Zhang, Y.; Miao, C.; Zhang, W.; Han, W.; et al. Stimulating the potential of Zn anode to operate in low pH and harsh environments for highly sustainable Zn batteries. *Angew. Chem. Int. Ed.* **2025**, *10*, e202419394. [CrossRef]
71. Li, X.L.; Qi, K.W.; Qin, Z.L.; Ding, X.; Zhu, Y.C.; Hou, Z.G.; Qian, Y.T. Ion-Anchored Strategy for MnO<sub>2</sub>/Mn<sup>2+</sup> Chemistry without “Dead Mn” and Corrosion. *ACS Nano* **2024**, *18*, 27016–27025. [CrossRef] [PubMed]
72. Zhang, F.; Wang, G.; Wu, J.; Chi, X.; Liu, Y. An Organic Coordination Manganese Complex as Cathode for High-Voltage Aqueous Zinc-metal Battery. *Angew. Chem. Int. Ed.* **2023**, *62*, e202309430. [CrossRef] [PubMed]
73. Li, C.; Yuan, H.; Liu, T.; Zhang, R.; Zhu, J.; Cui, H.; Wang, Y.; Cao, D.; Wang, D.; Zhi, C. Distinguish MnO<sub>2</sub>/Mn<sup>2+</sup> Conversion/Zn<sup>2+</sup> Intercalation/H<sup>+</sup>-Conversion Chemistries at Different Potentials in Aqueous Zn||MnO<sub>2</sub> Batteries. *Angew. Chem. Int. Ed.* **2024**, *63*, e202403504. [CrossRef]
74. Yao, H.; Dong, W.; Ji, X.; Cheng, S. Construction of self-standing MnO<sub>2</sub>-based films for reversible and practical electrolytic Zn//MnO<sub>2</sub> batteries in acidic environment. *Surf. Interfaces* **2024**, *44*, 103669. [CrossRef]
75. Wang, M.; Meng, Y.; Chen, N.; Chuai, M.; Shen, C.; Zheng, X.; Yuan, Y.; Sun, J.; Xu, Y.; Chen, W. Electrolyte Regulation of Bismuth Ions toward High-Performance Aqueous Manganese-based Batteries. *ACS Mater. Lett.* **2021**, *3*, 1558–1565. [CrossRef]
76. Gou, L.; Li, J.R.; Liang, K.; Zhao, S.P.; Li, D.L.; Fan, X.Y. Bi-MOF Modulating MnO<sub>2</sub> Deposition Enables Ultra-Stable Cathode-Free Aqueous Zinc-Ion Batteries. *Small* **2023**, *19*, 2208233. [CrossRef]
77. Qin, Z.M.; Song, Y.; Yang, D.; Zhang, M.Y.; Shi, H.Y.; Li, C.C.; Sun, X.Q.; Liu, X.X. Enabling Reversible MnO<sub>2</sub>/Mn<sup>2+</sup> Transformation by Al<sup>3+</sup> Addition for Aqueous Zn-MnO<sub>2</sub> Hybrid Batteries. *ACS Appl. Mater. Inter.* **2022**, *14*, 10526–10534. [CrossRef]

78. Li, Y.Q.; Zheng, X.L.; Carlson, E.Z.; Xiao, X.; Chi, X.W.; Greenburg, L.C.; Zhang, G.; Zhang, E.; Liu, C.W.; Yang, Y.F.; et al. In situ formation of liquid crystal interphase in electrolytes with soft templating effects for aqueous dual-electrode-free batteries. *Nat. Energy* **2024**, *9*, 1350–1359. [[CrossRef](#)]
79. Dai, C.; Hu, L.; Jin, X.; Wang, Y.; Wang, R.; Xiao, Y.; Li, X.; Zhang, X.; Song, L.; Han, Y.; et al. Fast constructing polarity-switchable zinc-bromine microbatteries with high areal energy density. *Sci. Adv.* **2022**, *8*, eab06688. [[CrossRef](#)]

**Disclaimer/Publisher’s Note:** The statements, opinions and data contained in all publications are solely those of the individual author(s) and contributor(s) and not of MDPI and/or the editor(s). MDPI and/or the editor(s) disclaim responsibility for any injury to people or property resulting from any ideas, methods, instructions or products referred to in the content.